A Computational Tool for the Reliable Prediction of Pavement Performance Based on Temperature Data

Ketson dos Santos, Principal Investigator
Civil, Environmental, and Geo- Engineering
University of Minnesota

December 2025

Research Report
Final Report 2025-40

To get this document in an alternative format or language, please call 651-366-4720 (711 or 1-800-627-3529 for MN Relay). You can also email your request to ADArequest.dot@state.mn.us. Please make your request at least two weeks before you need the document.

Technical Report Documentation Page

1. Report No.
MN 2025-40

2.

3. Recipients Accession No.

4. Title and Subtitle
A Computational Tool for the Reliable Prediction of Pavement Performance based on Temperature Data

5. Report Date
December 2025

6.

7. Author(s)
Ketson R. M. dos Santos, Mihai Marasteanu, Zifeng Zhao, Joao G. C. S. Duarte, Simon Custis

8. Performing Organization Report No.

9. Performing Organization Name and Address
Civil, Environmental, and Geo- Engineering
University of Minnesota
500 Pillsbury Drive S.E.
Minneapolis, Minnesota 55455

10. Project/Task/Work Unit No.
#2025032

11. Contract (C) or Grant (G) No.
(c) 1036342 (wo)138

12. Sponsoring Organization Name and Address
Minnesota Department of Transportation
Office of Research & Innovation
395 John Ireland Boulevard, MS 330
St. Paul, Minnesota 55155-1899

13. Type of Report and Period Covered
Final report

14. Sponsoring Agency Code

15. Supplementary Notes
http://mdl.mndot.gov/

16. Abstract (Limit: 250 words)
This study presents a computational tool for predicting pavement performance using long-term temperature data from thermocouple trees embedded in three flexible and two rigid pavement sections at the MnROAD facility. The research leverages spectral and probabilistic analyses to assess thermal behavior and its impact on pavement condition. Temperature measurements, supplemented by weather data, were processed to address missing data and artifacts using compressed sampling, ensuring a uniform 15-minute sampling interval. Spectral analysis techniques based on Fourier Transform and Wavelet Analysis with Generalized Harmonic Wavelets were used to model pavement layers as a cascade of filters, revealing the time-varying behavior of the filters' gain and phase shift, which indicates that they are sensitive to aging, moisture, and compaction. Wavelet analysis provided superior temporal resolution for detecting transient thermal phenomena. A probabilistic framework using Markov Chain Monte Carlo (MCMC) methods estimated thermal diffusivity coefficients, achieving residuals below 1.17°C and robust uncertainty quantification. The results highlight distinct thermal responses across pavement layers, with asphalt showing uniform behavior and base/subgrade layers exhibiting environmental sensitivity. Interfaces between layers displayed significant time-dependent changes, potentially linked to densification. Implemented as a modular Python package with Jupyter notebook examples, publicly available on GitHub, the tool offers a scalable solution for pavement monitoring. This research demonstrates that thermocouple-derived temperature data, when analyzed with advanced computational methods, provides reliable indicators of pavement degradation, supporting data-driven infrastructure management decisions.

17. Document Analysis/Descriptors
Pavement distress, Pavement performance, Temperature measurement, Data, Signal processing, Temperature sensors

18. Availability Statement
No restrictions. Document available from:
National Technical Information Services,
Alexandria, Virginia 22312

19. Security Class (this report)
Unclassified

20. Security Class (this page)
Unclassified

21. No. of Pages
79

22. Price

A Computational Tool for the Reliable Prediction of Pavement Performance Based on Temperature Data

Final Report

Prepared by:

Ketson R. M. dos Santos
Mihai Marasteanu
Zifeng Zhao
Joao G. C. S. Duarte
Simon Custis
Department of Civil, Environmental, and Geo- Engineering
University of Minnesota

December 2025

Published by:

Minnesota Department of Transportation
Office of Research & Innovation
395 John Ireland Boulevard, MS 330
St. Paul, Minnesota 55155-1899

This report represents the results of research conducted by the authors and does not necessarily represent the views or policies of the Minnesota Department of Transportation or the University of Minnesota. This report does not contain a standard or specified technique.

The authors, the Minnesota Department of Transportation, and the University of Minnesota do not endorse products or manufacturers. Trade or manufacturers' names appear herein solely because they are considered essential to this report.

ACKNOWLEDGEMENTS

This research study would not have been possible without the contribution of several organizations and individuals.

The research team would first like to acknowledge MN/DOT (Office of Materials & Road Research) as the lead state in this pooled fund study. The significant efforts of Dr. Ceren Aydin, Dr. Raul Velasquez, Joseph Podolsky, Dr. Bernard Izevbekhai are very much appreciated.

The research team would like to thank the members of the Technical Advisory Panel for their suggestions that helped improve the quality of this research effort. In particular, the suggestions offered by Dr. Ceren Aydin, Dr. Raul Velasquez, Joseph Podolsky, and Dr. Bernard Izevbekhai are much appreciated.

The research team would also like to thank Sanley Guerrier for his support in treating sensor data.

Table of Contents

List of Tables

List of Figures

Executive Summary

This study presents a data-driven approach to evaluating pavement performance using long-term temperature measurements from thermocouple trees embedded in pavement structures at the MnROAD research facility. The research focuses on three flexible and two rigid pavement sections equipped with vertical arrays of thermocouples that record subsurface temperature fluctuations over time. These measurements offer critical insight into the thermal behavior of pavement layers and their interaction with environmental conditions.

To address challenges related to missing or incomplete sensor data, a compressed sampling method was employed. Spectral analysis techniques—Fourier Transform and Wavelet Analysis—were used to extract frequency-dependent characteristics of heat flow, while a probabilistic framework based on the Markov Chain Monte Carlo (MCMC) method enabled the estimation of time-varying thermal diffusivities. The frequency response function (FRF) derived from these analyses provides a quantitative measure of each layer's thermal response, which can be used to detect changes in material properties due to aging, moisture infiltration, or compaction.

All computational methods were implemented in Python as a modular, object-oriented package and shared through a publicly accessible GitHub repository, along with reproducible examples in Jupyter notebooks. The findings demonstrate that thermocouple trees, when combined with robust spectral and probabilistic tools, can serve as reliable indicators of pavement condition, enabling the detection of degradation patterns and supporting long-term infrastructure management decisions.

List of deliverables

Deliverable	Description
Python codes	An oriented-object python package for the treatment, processing, and analysis of time-series.
Jupyter notebooks	Functional examples implemented in Jupyter notebooks.
Processed data	Image and data used to analyze the behavior of the different sections.

Chapter 1: Introduction

1.1 Background

The Minnesota Department of Transportation (MnDOT) and the University of Minnesota (UMN) have launched a collaborative data science initiative to leverage modern data analysis and machine learning techniques in support of pavement research and decision-making. Building on past MnDOT-UMN collaborations, this effort reflects MnDOT's broader commitment to innovation and data-driven practices in pavement engineering, infrastructure management, and policy planning.

Transportation agencies increasingly depend on large-scale sensor data, vehicle tracking systems, and other digital monitoring tools to evaluate infrastructure performance. However, converting these vast datasets into actionable insights remains a significant challenge. In response, MnDOT has partnered with UMN researchers to advance the use of data science and machine learning methods to predict pavement performance using temperature data. The collaboration focuses on improving the interpretability, quality, and utility of MnDOT's Long-Term Pavement Performance (LTPP) datasets through targeted research aligned with current agency priorities.

This project encompasses work conducted in 2024 and 2025 and builds on outcomes and lessons learned from previous efforts. The proposed work emphasizes the continued refinement and application of data processing pipelines, validation of data quality and trends, and the development of exploratory and predictive analytics tools to support MnDOT's operational and research objectives.

1.2 Objectives

The primary objective of this project is to support MnDOT's use of data science techniques to analyze and enhance the quality and utility of its transportation-related datasets. The research team aims to develop and refine methods for exploring large-scale sensor data, identifying meaningful patterns, and detecting anomalies or changes over time. This includes building pipelines to clean, preprocess, and organize raw data into formats suitable for further analysis. In addition, the team evaluates the consistency, completeness, and reliability of MnDOT's datasets. Tasks include creating tools to visualize data gaps, outliers, and other quality issues, as well as establishing metrics to flag problematic data entries. Furthermore, the team seeks to implement spectral and probabilistic analysis methods to identify trends, support forecasting, and extract actionable insights from complex datasets.

Chapter 2: Literature Review

This chapter presents a comprehensive literature review of pavement monitoring tools and methods that utilize thermal data. The review covers the relationship between pavement materials and thermal conduction, modeling approaches for pavement thermal conditions, sensing technologies, and computational methods for pattern recognition in pavement monitoring data.

2.1 Sensor Technologies in Pavement Monitoring

Plankis and Heyliger (2013) identified four levels of damage identification for evaluating pavement conditions using sensor technology: detection of damage presence, localization of damage, assessment of damage severity, and prediction of the remaining service life of the structure. To address the first three levels, Yang (2014) categorized pavement condition monitoring into two types: global and local monitoring. The characteristics of these two approaches are summarized in Table 2.1. Current applications of pavement condition monitoring primarily rely on local monitoring techniques, in which wired or wireless sensors are embedded in the pavement structure to capture long-term strain and temperature variations resulting from combined traffic and environmental effects.

Table 2.1 Characteristics of global and local pavement monitoring

Properties	Global monitoring	Local monitoring
Model properties	• Resonant frequency, • Mode-shape vectors/curvatures, • Dynamic flexibility matrix, • Acoustic properties	• Track damage progress, • Evaluation damage detection, • Cracks, defects, etc.
Examples	• Unmanned aerial vehicles (UVA) based LiDAR, • IRI measurement via vehicle-mounted sensors	• Sensors and gauges, • Thermocouples, moisture probes.
Data resolution	Lower resolution, general condition assessment	High resolution, detailed structural analysis
Cost	Generally lower cost per mile	Higher cost due to labor and equipment
Key applications	Pavement management systems	• Structural evaluation, • Maintenance planning, • Forensic investigations

2.1.1 Wired Sensor Applications

Wired sensors have become an integral tool in pavement engineering, enabling real-time monitoring and assessment of pavement conditions. These sensors are embedded within or mounted on pavement structures to collect critical data on parameters such as strain, temperature, moisture, pressure, and deflection. Common types of wired sensors used in pavement monitoring include strain gauges, linear variable differential transformers (LVDTs), fiber optic sensors, piezoelectric sensors, and thermocouples. Since temperature measurements significantly influence pavement structural responses, they are often paired with strain or displacement measurements to enable accurate interpretation and modeling of mechanical behavior.

Wired sensors are typically installed during pavement construction or through post-installation methods such as coring. In post-installation, a core is drilled into the pavement, the sensor is placed inside, and the hole is sealed with resin to prevent sensor displacement (Barriera et al., 2020). These sensors are connected to data acquisition systems via physical cables that transmit the collected data to centralized monitoring units for analysis. This wired configuration ensures reliable, high-fidelity data transmission, making it well-suited for long-term pavement performance monitoring. Table 2.2 summarizes the unique mechanisms, functions, and specific applications of various wired sensors, offering a comprehensive overview of their roles in pavement engineering.

Table 2.2 Comparison of wired sensors for pavement condition monitoring

Sensor type	Example	Function	Mechanism
Strain gauges	Electrical resistance strain gauges	Measure strain in pavement layers under loads	Measures electrical resistance change when strained
Linear variable differential transformer sensors (LVDT)	Displacement transducers	Measures pavement deflection and displacement	Uses magnetic induction to detect linear displacement
Fiber optic sensors	Fiber Bragg grating (FBG) sensors	Measures strain, temperature, and cracks in pavement	Uses light reflection and wavelength shifts in optical fibers to measure strain and temperature
Temperature sensors	• Thermocouples, • Resistance temperature detectors (RDTs)	Assess thermal effects on pavement durability and ageing	• Thermocouples: voltage changes due to temperature difference, • RDTs: electrical resistance changes with temperature
Moisture sensors	Time-domain reflectometry sensors	Evaluates moisture damage and drainage efficiency	Sends and electrical signal into the ground and measures the reflection time

Zhao et al. (2014) developed monitoring system for the runway of Shanghai Pudong International Airport with strain gauges, multi-depth deflectometers, temperature and moisture sensors. From site experiences, it was suggested that optical technology ought to be used in the system because optical sensors delivered signals for long distances without signal loss. When installing the sensor in cement concrete runway, Zhao et al. (2014) suggested that all sensors should be installed on a frame and fixed on the base, to protect the sensors and keep the location.

Cook et al. (2016) used strain gauges and thermocouples to determine the interlayer delamination at the intersection of Runway 4 R-22L and High-Speed Taxiway N (HST-N) at Newark Liberty International Airport. A critical signal indicator, Δε, which is the peak difference on the micro-strain curve, was selected as delamination-evident events, as presented in Figure 2.1. The total distributions of responses for all strain gauges were analyzed using the Kolmogorov-Smirnov test to compare the Δε values between delamination and non-delamination evident responses. Results showed that the Δε values for the bonded events were statistically different with a degree of confidence of over 99.9%.

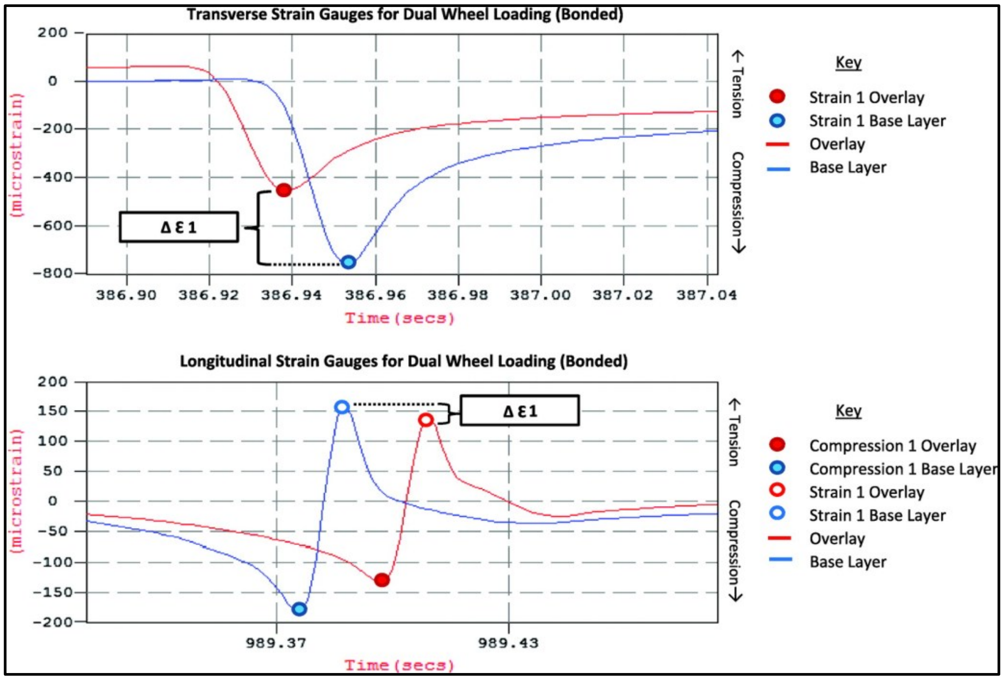

Figure 2.1 Use of Δε as delamination evidence during strain data recognition (Cook et al. 2016)

Duong et al. (2019) used strain gauges, temperature probes, and geophones to continuously monitor an asphalt pavement motorway for 18 months. The mechanical response was analyzed using both a classical multi-layer linear elastic pavement model and a viscoelastic model. The results showed that the pavement response exhibited significant variations with temperature. Notably, the degree of bonding between layers tended to decrease at high temperatures. In their analysis, Duong et al. (2018) also employed signal processing methods to select low-noise signals.

Liu et al. (2021) analyzed the dynamic strain response of a typical asphalt pavement using fiber Bragg grating sensing technology. The fiber Bragg grating demodulator had a data sampling frequency of 1 kHz, enabling the timely collection of strain data. The results indicated that the longitudinal strain at the bottom of the surface courses under dynamic loading followed a compressive–tensile–compressive alternating pattern. The peak of the dynamic strain response decreased with increasing depth of the surface course and increased with the thickness of the base course.

Zhao et al. (2022) investigated the long-term strain characteristics of rubberized asphalt pavement containing reclaimed asphalt pavement (RAP) using an accelerated pavement tester. Strain sensors were embedded at the bottom of the surface layer. Within 700,000 wheel passes, it was observed that the maximum strain after 100,000 passes accounted for over 70% of the maximum strain recorded during the final loading cycle. For strain under the wheel tracks, horizontal strain demonstrated better recovery than vertical strain.

Zhao et al. (2023) compared the strain characteristics of flexible, semi-flexible, and rigid pavements under accelerated loading. They found that with an increasing number of accumulated wheel passes, flexible pavements exhibited the largest transverse micro-strain, while semi-flexible pavements showed the largest longitudinal strain. Correlation analyses revealed that the maximum micro-strain had a strong exponential relationship with the maximum rutting depth across all pavement types.

Liu et al. (2024) conducted structural health monitoring on asphalt pavements using resistive sensors and fiber optic Bragg grating sensors. Two types of external loading—an accelerated pavement testing machine and a stationary falling weight—were applied to monitor strain at various pavement depths. To ensure data accuracy, the moving average method was used in signal processing. Additionally, it was noted that strain accumulated during the initial loading stage and produced a peak phase difference in the response. Liu et al. (2024) emphasized the necessity of subtracting baseline-adjacent data from the sensor output time history to obtain a corrected signal response curve.

2.1.2 Wireless Sensor Applications

The complex layout and installation requirements of thermocouple systems can limit their practical application in large-scale field monitoring, even though they are generally more cost-effective than wireless sensors. Additionally, fiber sensors are susceptible to breakage during construction and compaction. In contrast, online monitoring techniques—made increasingly attractive by advances on the Internet of Things—can overcome the limitations of wired sensor systems through their high flexibility.

Wireless sensors offer distinct advantages in large-scale or hard-to-access pavement networks, where installing wired systems may be impractical or prohibitively expensive. Their ability to function without physical connections reduces the risk of damage during construction and enhances long-term reliability. Furthermore, wireless systems support scalable and adaptable monitoring solutions, making them suitable for both research and practical applications. Commonly used wireless sensors in research and field applications are listed in Table 2.3.

Table 2.3 Comparison of wireless sensors for pavement condition monitoring, mechanisms

Sensor type	Measurement parameters	Advantages	Limitations	Mechanism
Micro-electro-mechanical systems (MEMS)	• Strain, • Acceleration, • Displacement, • Pressure	Small size, low power, consumption, real-time data	Sensitivity to environmental factors, potential drift over time	Uses microscale mechanical components and electrical signals
Wireless strain gauges	• Strain, • Stress	No wiring needed, long-term monitoring capability	Limited battery life requires calibration	Converts strain into electrical resistance changes, transmits wirelessly
Piezoelectric sensors	Traffic load and vibration	High sensitivity, energy harvesting potential	Limited accuracy in long-term applications	Converts mechanical stress into an electrical charge

Sensor type	Measurement parameters	Advantages	Limitations	Mechanism
Radio frequency identification (FRID)-based sensors	• Crack propagation, • Displacement	Low power consumption and low maintenance	Short reading range for passive RFID	Uses passive or active RFID signals to transmit data

To estimate truck weight under different pavement temperatures and varying environmental conditions, Bajwa et al. (2013) developed a wireless sensor network consisting of acceleration sensors and vehicle detection sensors. The network was installed on a cement concrete pavement. Using a composite one-dimensional Euler beam on Winkler foundation model, Bajwa et al. (2013) developed a layered elastic theory model to simulate the effect of temperature on pavement response, enabling the estimation of axle loads through pavement vibrations. The system achieved an accuracy of 15% for individual axle loads and 10% for total load, outperforming a nearby conventional Weigh-In-Motion (WIM) system.

Ceylan et al. (2016) evaluated the early-age curling and warping behavior of cement concrete pavement using commercial off-the-shelf micro-electromechanical systems (MEMS). During the monitoring period, in addition to capturing weather and seasonal variations, the data accurately reflected events such as thunderstorms, heat waves, and seasonal temperature changes. However, in terms of sensor durability, it was found that more than 70% of the embedded sensors remained functional one month after the pavement was opened to traffic, while only 20% were still operational ten months after opening.

Hasni et al. (2017) employed self-powered wireless sensors with non-constant injection rates to detect bottom-up cracking in asphalt concrete pavements. Sensor performance was evaluated through numerical and experimental studies on asphalt concrete specimens subjected to three-point bending. Crack detection was based on voltage amplitude deviations caused by damage events. It was observed that the slope of the strain/voltage versus number of applied cycles curves increased as damage progressed. Hasni et al. (2017) suggested that the percentage drop in voltage/strain could serve as a reliable indicator of damage progression, while gate number and activation were good indicators of damage severity.

Bajwa et al. (2020) developed a cost-effective pavement performance assessment method using a wireless accelerometer system. Embedded in the road, the wireless sensor measured transient vibrations caused by applied loads to assess pavement displacement. A developed algorithm enabled direct evaluation of pavement condition and performance based on vibration data. Additionally, displacement data could be used to back-calculate pavement layer stiffness, facilitating long-term performance prediction.

Shi et al. (2021) estimated vehicle speed from pavement stress responses using a novel wireless micro-electromechanical sensor. An indoor accelerated pavement testing machine was used to replicate traffic loading patterns. The MEMS sensor reliably captured real-time stress-response data from the asphalt pavement. Using a loading interval approach, vehicle speed could be estimated based on stress wave timing. The study suggested using the predominant frequency method for speed estimation in mixed and complex traffic conditions.

Zhang et al. (2024) developed an in-situ dynamic modulus prediction model using a neural network trained on real-time sensing data. The SmartKli aggregate-sized wireless sensor was used to collect mechanical response data, including triaxial stress, acceleration, Euler angles, and temperature. Data were transmitted to the adapter system via Bluetooth Low Energy. The sensor's external shell, made of 3D-printed high-strength ABS nylon, demonstrated sufficient durability to withstand asphalt compaction temperatures ranging from 120°C to 150°C.

2.2 Pavement Condition and Thermal Property

Traditional structural health monitoring approaches for highway pavement infrastructure systems often involve full-scale test tracks instrumented with numerous sensors, such as strain gauges, pressure cells, displacement gauges, subgrade moisture sensors, and others. The primary motivation for constructing and operating a full-scale pavement test track is to study pavement response and behavior under realistic yet controlled conditions (Hugo and Epps, 2004). Table 2.4 summarizes the common types of sensors used in various test tracks.

Table 2.4 Sensors used in traditional pavement health monitoring

Projects	Monitoring Systems	Year	Reference
MnROAD	• Over 9,500 sensors, • Including Linear Variable Differential Transformer (LVDT), • Strain gauges, dynamic soil pressure cells, • Moisture gauges, thermocouples etc.	1991	(Tompkins and Khazanovich, 2007)
Virginia Smart Road	• Over 400 sensors, • Including weight-in-motion sensors (WIM), • Temperature, strain, vibration sensors.	1997	(Al-Qadi et al. 2004)
NCAT Test Track in Auburn University	• Copper-based strain gauges temperature sensors, • Soil pressures, soil moisture sensors.	2000	(Timm et al., 2004)
Maine DOT	• Over 50 sensors, • Including strain gauges, thermocouples, • Soil strain gauges, soil pressure cells, • Soil moisture gauges, frost resistivity probes.	2005	(Swett et al. 2008)
French Highway A41N	• Over 40 sensors, • Including strain gauges, temperature probes.	2012	(Gaborit et al. 2013)
SMARTVIA	• Over 90 sensing technologies, • Including temperature sensors, strain gauges, moisture tubes.	2014	(Pouteau et al. 2016)

Yavuzturk et al. (2005) developed a transient, two-dimensional finite-difference model to assess temperature fluctuations in asphalt pavements caused by thermal environmental conditions. The various asphalt layers were represented using a 25 mm grid increment in the direction normal to the pavement surface, with variable specifications for the thermal and radiative absorptivity of asphalt mixes, surface convective conditions, and solar radiation. The study found that pavement thermal response was strongly influenced by climate conditions, the thermal and radiative properties of asphalt mixtures, surface convective conditions and geometry, and solar radiation. In contrast, the length and orientation of the asphalt segment had an insignificant effect.

Yang (2014) used RFID tags and thermocouples to monitor temperature variations in a newly constructed jointed plain concrete pavement on U.S. Highway 30 from May 24, 2013, to April 1, 2014. RFID tags were deployed both in extended configurations to enhance transmission signals and in embedded configurations to ensure accurate temperature readings. All iButton thermocouples were embedded. Results showed that both RFID tags and thermocouples successfully captured the sharp temperature rise caused by the cement hydration reaction during the initial stage of concrete paving.

DeDene et al. (2016) measured the thermal conductivity of reclaimed asphalt pavement (RAP) using a custom-built laboratory apparatus. As shown in Figure 2.2, the main components of the setup included two aluminum plates, each measuring 10 × 10 inches in area and 0.25 inches thick. These plates served as heat spreaders, providing uniform temperature boundary conditions on the top and bottom surfaces of the test specimen, which was placed between them. Sheet-type rubberized heating pads powered by an adjustable DC voltage source were attached to the rear face of each aluminum plate. A calibrated heat flux meter and a micro-thermocouple were affixed to the center of the front face to monitor heat transfer. Thermal conductivity was measured for RAP particles with the asphalt binder removed, as well as for pure asphalt binder subjected to varying degrees of aging. Results indicated that the thermal conductivity of the solid media was influenced by three key factors: (a) particle size distribution, (b) sample density, and (c) sample porosity. The thermal conductivities of the solid media ranged from 17 to 30 W/m·°C, while those of the asphalt binder ranged from 0.17 and 0.19 W/m·°C.

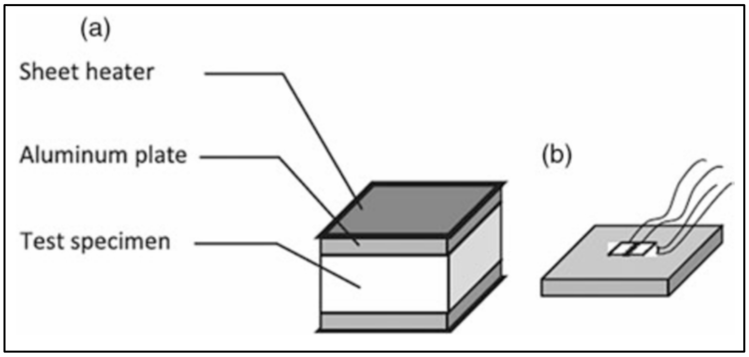

Figure 2.2 Schematic diagram of the experimental apparatus (DeDene et al. 2014)

Hassan et al. (2016) investigated the influence of air void content on the thermal properties and temperature evolution of asphalt mixtures under both dry and wet conditions. Asphalt concrete slabs measuring 306 × 306 × 50 mm were prepared using a laboratory roller compactor at air void contents of 4.5%, 13.0%, 17.0%, 21.0%, and 26.0%. A heat flux transducer and a J-type thermocouple were used to measure the heat conducted through the asphalt slabs. The study found that asphalt mixtures with lower air void content exhibited higher thermal conductivity. Under wet conditions, the thermal conductivity of the asphalt mixture dropped sharply once the water available for evaporation was depleted.

Li et al. (2018) developed a temperature prediction model that accounts for the cumulative effects of air temperature and solar radiation. At five different sites, thermocouples were installed to measure pavement temperatures at various depths. Using the collected data, relationships between cumulative time and depth were established and modeled as segmented linear regression functions. Based on these models, empirical temperature prediction equations were proposed. As shown in Figure 2.3, the temperature prediction model is expressed as a linear combination of average air temperature and total solar radiation. The weighting of average temperature is relatively small near the pavement surface but increases with depth, whereas the influence of total solar radiation decreases with depth.

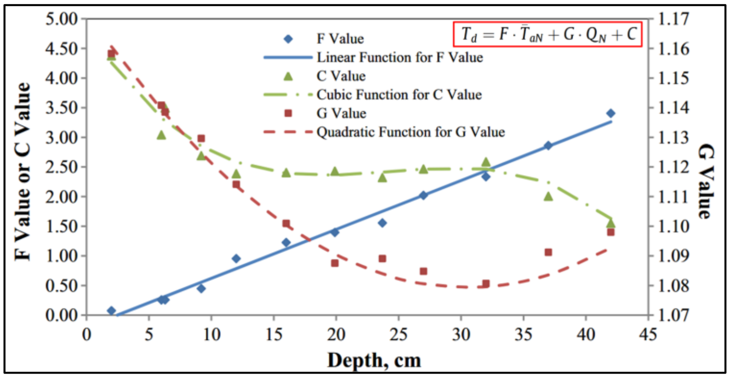

Figure 2.3 Relationship between depth and coefficients

Godoy et al. (2018) utilized a set of prototype probes to capture temperatures at various pavement depths. Equipped with vehicle-to-infrastructure communication capabilities, auscultation vehicles were able to measure temperatures at multiple depths without stopping for drilling or direct surface measurements. The collected temperature data were used to verify the BELLS3 temperature model and to develop a neural network–based model for predicting pavement temperatures. Based on a year’s worth of data, the study demonstrated that the neural network model outperformed the traditional BELLS3 model in predicting pavement temperatures.

Teltayev and Suppes (2019) employed temperature and moisture sensors to examine temperature variation and its influence on moisture distribution in the pavement and subgrade of a highway. As shown in Figure 2.4, they observed considerable noise in the temperature signals and identified similar variation trends between pavement and air temperatures. They concluded that the greater the absolute value of air temperature, the larger the discrepancy between air and pavement surface temperatures. In hot and warm seasons, this discrepancy is attributed to the dark color of asphalt concrete, which absorbs thermal radiation. In contrast, during the cold season, heat flow moves upward from the bottom layers due to the presence of a temperature gradient. Additionally, they found that daily temperature variation was absent at a depth of 35 cm, while at greater depths (140 cm and beyond), temperature variation occurred primarily on an annual cycle.

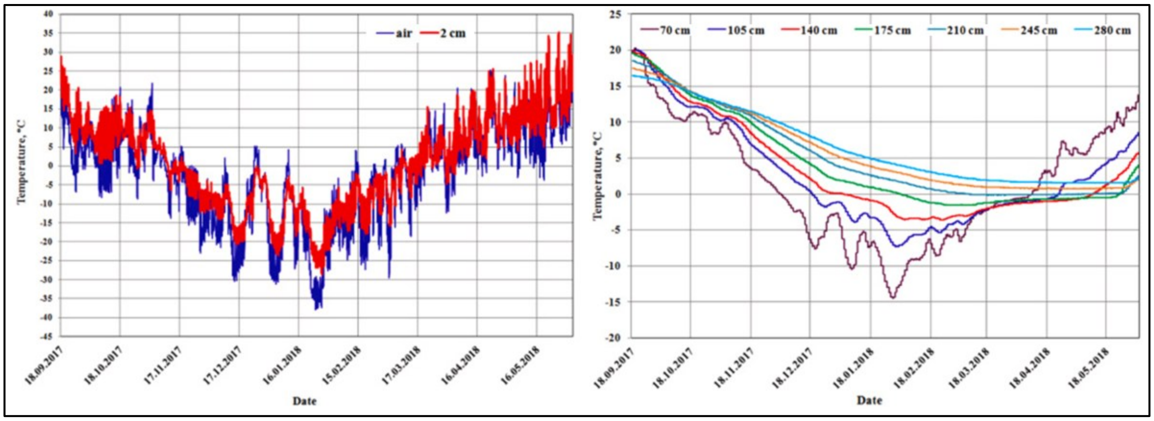

Figure 2.4 Variation of air temperature and temperature in asphalt concrete pavement (Teltayev and Suppes, 2019)

Using thermal cameras, Golrokh et al. (2021) developed an integrated system that combined infrared imaging, high-resolution visual imaging, real-time image processing, and data-rich analytics to evaluate pavement surface distress. Pavement cracks were characterized by measuring depths and widths with a digital caliper. Temperatures (in Kelvin) were normalized based on the mean temperature of the surrounding undamaged area and then correlated with crack depth and width measurements. A 70% reliability was found in the correlation between pointwise normalized temperature and crack depth; however, the correlation between crack width and normalized temperature was deemed unreliable.

Ma et al. (2023) employed the SmartRock sensor for pavement health monitoring. Using the monitored modulus and temperature data, they proposed an improved genetic algorithm for back-calculating the pavement's dynamic modulus. The evaluated moduli were then used to predict the residual rutting life and residual fatigue life of the pavement structure. To prolong the service life of SmartRock, Ma et al. (2023) suggested two approaches: (1) harvesting vibration energy using piezoelectric materials to generate electricity, and (2) setting the sensor to sleep mode when no vehicle is present.

Podolsky et al. (2023, 2024) conducted a statistical analysis to assess the feasibility of using pavement temperature as a surrogate for performance prediction in both flexible and rigid pavements. Data were collected from thermocouple arrays embedded within the pavement structure. Various data science techniques—including natural neighbor interpolation, retiming, and linear regression modeling—were applied to an extensive dataset. For rigid pavements, thermocouple data were able to identify periods of excess moisture within the concrete layer and detect potential damage near pavement joints. For flexible pavements, air temperature was identified as the most significant predictor of pavement temperatures recorded by thermocouple sensors. Moreover, the embedded thermocouples served as indicators of changes in distress growth rates in flexible pavements.

Initially, this section aimed to gather literature on how pavement condition could be assessed through thermal properties such as thermal conductivity, heat transfer characteristics, and pavement albedo. The goal was to understand how these properties correlate with pavement distress and overall structural integrity. However, a comprehensive review revealed that few studies have specifically investigated the impact of distress on the thermal conductivity of pavement materials. Most existing research focuses on general pavement thermal behavior rather than how cracks, moisture infiltration, oxidation, or aging influence heat transfer properties. This gap in the literature underscores the novelty and significance of the current project. Understanding how distress alters thermal conductivity could add a new dimension to pavement condition monitoring, potentially improving predictive maintenance strategies and enhancing the accuracy of non-destructive evaluation methods. Given the growing interest in using thermal imaging and remote sensing for infrastructure assessment, further investigation in this area is both timely and necessary.

2.3 Thermal Condition Modeling Approaches

To model pavement temperature, Hermansson (2001) developed a finite-difference approximation model that considered convection, shortwave radiation, and longwave radiation. The model's inputs included hourly values of solar radiation, air temperature, and wind velocity. For heat transfer calculations, the porosity and degree of water saturation in the layers below the pavement surface were also incorporated. Validation using data from 12 different sections of the Long-Term Pavement Performance (LTPP) program showed an average error of less than 2°C for both asphalt concrete and cement concrete pavements. When model parameters were individually adapted to each section, the average error decreased to approximately 1°C.

Herb et al. (2009) developed a one-dimensional finite difference heat transfer model to characterize pavement temperature variations on both diurnal and seasonal timescales. The model captured daily extreme temperatures, temperature gradients, diurnal cycling, and seasonal fluctuations. Results indicated that surface temperature gradients could reach up to 5 °C/cm, and the rate of temperature change could be as high as 40 °C/hour. Regarding diurnal temperature variations, the amplitude generally increased with rising mean temperatures; however, significant amplitudes were also observed under cold conditions.

Alavi et al. (2014) proposed an alternative approach for predicting pavement temperature profiles using the finite control volume method. The partial differential equation of heat diffusion, along with surface and bottom boundary conditions, was solved using this method. In the model, control volumes at the pavement surface and bottom were aligned with the physical domain boundaries. Discontinuities in thermal properties within multilayer pavement systems were addressed by assigning appropriate properties to each control volume. These improvements enabled accurate temperature profile predictions at two LTPP sites: LTPP040113 in Kingman and LTPP300114 in Great Falls.

Qin and Hiller (2014) simulated pavement systems with varying albedo levels and thermal inertia to evaluate the effects of surface and heat-storage modifications on instantaneous and cumulative sensible heat. They found that most absorbed heat was discharged as sensible heat and longwave radiation, while cumulative daily heat conduction accounted for approximately 5% of the absorbed energy. Results suggested that increasing surface albedo and enhancing evaporative flux were effective strategies for suppressing sensible heat and promoting cooler pavements.

Chen et al. (2019) reviewed theoretical models for temperature prediction and critical influencing factors. They noted that the finite difference method (FDM) and finite volume method (FVM) could be computationally more efficient than the finite element method (FEM), though FEM and FVM were more suitable for complex geometries. Regarding key climatic and pavement-related inputs, shortwave radiation at the pavement surface could be either measured or calculated using the solar constant and sun position. The convective heat transfer coefficient was typically derived from empirical equations involving wind speed. Net longwave radiation could be estimated via sky temperature or approximated using a factor representing surface absorptivity instead of emissivity. The authors emphasized the need to calibrate empirical equations and account for pavement surface material and age when determining albedo and emissivity. For example, asphalt pavement albedo increases over time as its color fades from black to lighter tones, whereas concrete pavement albedo initially rises with cement hydration but stabilizes within six weeks and later declines due to weathering.

Sun et al. (2020) developed a microstructure-based multiscale finite element method to investigate the impact of temperature fields on damage initiation in asphalt pavement under traffic loading. The model incorporated thermal radiation, convection, and conduction mechanisms. Mechanical and thermal properties at both the pavement and mixture levels were integrated through a homogenization process. Digital image processing was used to construct representative volume elements (RVEs) of the asphalt concrete microstructure, and a bilinear cohesive zone model was applied to simulate damage initiation within these RVEs. The results demonstrated that the multiscale model provided valuable insights into the damage behavior of asphalt pavement under varying thermal conditions at both macroscopic and microscopic scales.

Yelizarov (2023) developed a one-dimensional numerical heat transfer model incorporating snowmelt processes and tree shade effects to predict pavement surface temperature. The model was validated using historical weather data and thermocouple measurements. Although prediction accuracy was lower over a six-month period, the model performed well over a 10-hour window with minimal precipitation and a thin, dry snowpack. The average error compared to thermocouple measurements was 1.525%, with a root mean square error of 0.1525.

2.4 Computational Approaches for Data Pattern Recognition

Pavement condition assessment increasingly relies on sensor-derived signals to evaluate structural integrity, layer thickness, and subsurface defects. These signals, however, are often contaminated by what is traditionally considered “noise,” resulting from environmental interference, sensor inaccuracies, or mechanical vibrations. While some of this noise may obscure critical features. It is important to recognize that not all noise is meaningless, certain signal irregularities may carry valuable information about internal damage mechanisms or evolving structural deterioration.

Signal processing techniques play a pivotal role, not only in enhancing the signal-to-noise ratio to clarify dominant features, but also in preserving or isolating potential damage-related patterns embedded within the noise. Techniques such as wavelet denoising adaptively filter high-frequency components while preserving transient peaks associated with structural reflections. Kalman filtering provides dynamic signal estimation in real-time settings, allowing for the integration of sensor uncertainty and system dynamics. Fourier transform-based bandpass filtering removes out-of-band interference, and matched filtering enhances known signal patterns.

For peak detection, envelope analysis and Hilbert transform-based demodulation are used to emphasize amplitude modulations in vibration signals, aiding in the identification of resonant frequencies associated with pavement degradation. This section explores signal processing methodologies specifically tailored to pavement engineering applications, with a focus on robustness in noisy environments and their role in converting raw sensor data into actionable indicators of structural health.

2.4.1 Probabilistic Methods

Unlike deterministic models that provide an exact serviceability value or pavement condition index based on historical data, probabilistic analysis and prediction models estimate pavement performance by assigning probabilities to different condition states. These models describe the potential outcomes of the pavement's condition as a random process (Durango, 2002).

Gharaibeh and Darter (2003) applied survival analysis—a statistical method widely used in actuarial research—to determine the distribution of service lives and life expectancy for 1,402 Interstate and freeway sections in Illinois. Survival analysis is more appropriate than calculating a simple average life, especially when not all sections in the dataset have reached the end of their service lives. Both pavement age and traffic loading were found to influence survivability and were thus incorporated into the analysis, as shown in Figure 2.5.

The survival curves were generated using the LIFETEST procedure in SAS software. Each data point on the curves represents the probability that a given pavement section will be overlaid upon reaching a specific age or cumulative ESAL (Equivalent Single Axle Load). The results in the figure indicate that D-cracking significantly affects pavement performance, with performance reductions ranging from 32% to 63% compared to non-D-cracked pavement.

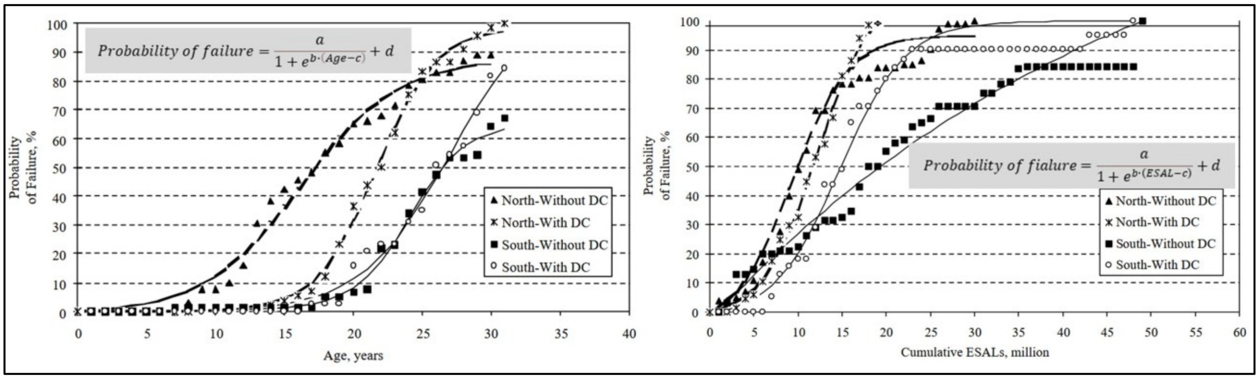

Figure 2.5 Survival curves for age and ESAL for 10-in. JRCP (Nasir and Michael, 2003)

Li and Zhang (2007) proposed an ordered probit model and a sequential logit model to predict pavement conditions. The ordered probit model was used to construct a discrete pavement performance model, in which the observed pavement condition state was assumed to be linked to an underlying latent pavement performance propensity. The sequential logit model, on the other hand, determined the condition state through a series of independent binary response models, where a pavement section transitions to the condition state with the highest utility. These probabilistic models were pilot-tested using pavement performance data from the AASHTO Road Test, yielding promising prediction results.

Luo and Yin (2008) developed a cluster-wise regression model for pavement families to evaluate pavement distress ratings. They assumed that each pavement family dataset could be further divided into several clusters, each represented by a unique regression equation. Each cluster corresponded to a portion of the dataset that exhibited a consistent trend. A weighted regression function incorporating all clusters was introduced to account for both current and historical observations. At the network level, the proposed model significantly outperformed the conventional Markov model in terms of prediction accuracy.

Recognizing that traditional deterministic models may not fully account for the influence of weather and traffic on pavement distress, Saha et al. (2017) employed a discrete-time Markov process to develop probabilistic prediction models for five distress indices: transverse cracking, longitudinal cracking, fatigue, rutting, and ride. An initial transition probability matrix—representing the likelihood that a pavement segment remains in a given condition state for a year—was established. Future condition states were then predicted by multiplying the initial state vector by the transition probability matrix raised to the power of t, where t is the number of years into the future. Although the Markov model captures condition changes probabilistically, it assumes the Markov property, that future states depend only on the current state, which may limit its ability to reflect the cumulative effects of prior conditions.

An example of a Markovian deterioration model is shown in Figure 2.6. In a case study of low-volume roads in Colorado, 116 roads (totaling 2,022 miles) were segmented into 342 sections to create the dataset. Results showed that longitudinal cracking, fatigue, and rutting indices exhibited minimal deterioration over time, while transverse cracking and ride quality indices deteriorated more rapidly.

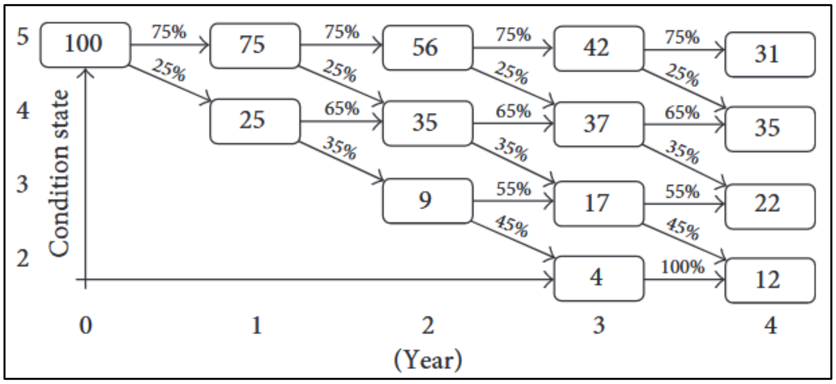

Figure 2.6 Example of a Markovian deterioration model (Saha et al. 2017)

Hassan et al. (2017) developed pavement surface distress deterioration models using logistic regression and Markov chains, with distress rating and surface age as model variables. Pavement condition data were collected through visual inspection. Upon comparison, it was found that for the network modeled, the logistic regression models produced predictions that closely matched the actual average condition data across various pavement ages. Additionally, it was observed that predictions from most Markov chain models were higher than those from the logistic models and the actual average condition data.

Yamany and Abraham (2021) introduced and validated a hybrid approach to incorporate the effects of preventive maintenance into probabilistic pavement performance models, particularly in cases where historical preventive maintenance data were unavailable. They developed a nonhomogeneous Markovian pavement model by estimating transition probabilities using the ordered probit method. The hybrid approach and resulting performance models were validated through cross-validation with out-of-sample data and expert surveys conducted with pavement engineering professionals. Results indicated that the hybrid approach predicted pavement condition, including the effects of preventive maintenance, with an accuracy of 87%.

2.4.2 Spectrum Analysis

Spectrum analysis of sensor data—particularly through techniques like Fourier Transforms and Short-Time Fourier Transforms (STFT)—has become a key method for extracting meaningful patterns from complex datasets.

Bajwa et al. (2011) developed a wireless sensor network using vibration sensors embedded in pavement to classify vehicles based on axle count and spacing. Although the study does not explicitly describe the use of spectrum analysis, the reliance on vibration data for classification likely involves frequency-domain techniques, given the common application of Fourier analysis in such contexts. This approach is significant for traffic monitoring and pavement load assessment, with potential implications for predicting pavement wear.

Yan et al. (2020) conducted a field experiment on in-service pavements to characterize surface texture using spectral analysis, correlating the findings with friction values. Texture spectra were analyzed using third-octave bands, with key correlations identified at wavelengths between 1.25 and 12.5 mm for friction at speeds of 60 and 80 km/h. The study employed a stationary laser profilometer, highlighting the effectiveness of spectrum analysis in evaluating pavement safety and performance.

Al-Omari et al. (2021) carried out a study on forecasting flexible pavement temperatures using Fourier series formulas in MATLAB. A total of 216,086 observations spanning a 26-year period (1991–2016) were analyzed on daily, monthly, and annual scales. A localized Fourier series approach was used to capture thermal trends over time: 36 Fourier series formulas were developed to predict maximum, minimum, and average monthly air temperatures for specific months and years; 9 formulas were created for daily predictions; and 3 for overall monthly estimates. The predicted temperatures were linked to Strategic Highway Research Program (SHRP) models for selecting performance-grade asphalt binders, demonstrating the utility of Fourier methods for long-term temperature forecasting (as shown in Figure 2.7).

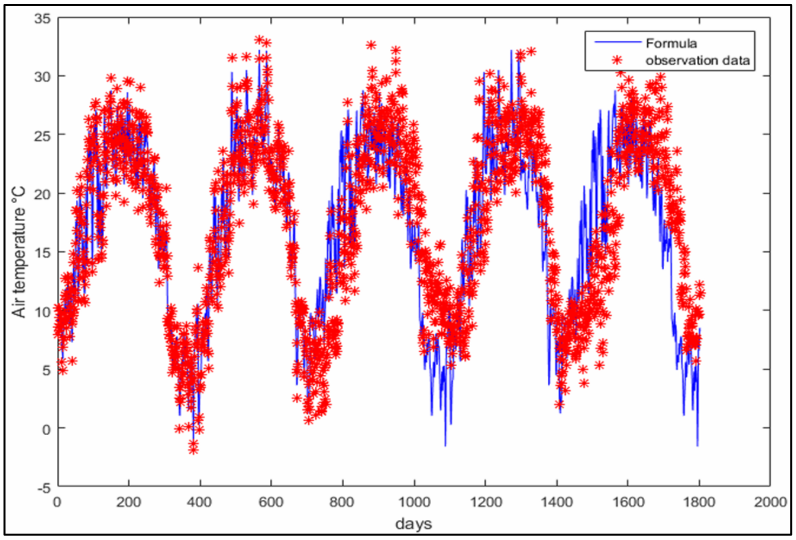

Figure 2.7 Validation of the two-year average temperature formula with observation data recorded over five years (Al-Omari et al. 2021)

Wu et al. (2025) introduced a deep learning model that integrates a spectrum-focused transformer layer for pavement distress recognition. The transformer layer processes signal spectra using the Fast Fourier Transform, concentrating on critical frequency components to enhance the detection of distress regions. Experiments conducted on a road pavement distress dataset achieved a test accuracy of 97.73%, demonstrating the effectiveness of combining spectrum analysis with deep learning. This approach is particularly notable for its ability to capture complex patterns, with ablation experiments indicating a 0.98% improvement in accuracy over baseline models.

To facilitate a structured comparison, Table 2.5 summarizes the spectrum analysis methods, their advantages, optimal applications in pavement engineering for long-term sensor data, and relevant references.

Table 2.5 Spectrum analysis methods, advantages, and applications

Method	Advantages	Best suited for	References
Fourier Transform (FT)	• Efficient for stationary signals, • Good for identifying periodic components.	• Temperature data with regular cycles, • Long-term data where the signal is relatively stable	(Al-Omari et al. 2021)
Short-Time Fourier Transform (STFT)	• Handles non-stationary signals, • Tracks frequency changes over time.	• Strain data from dynamic loads (traffic) • Moisture data with varying patterns	(Qiao and Qin, 2018)
Wavelet Transform	• Better time-frequency localization than STFT, • Suitable for signals with abrupt changes.	• Pavement texture analysis • Strain data with sudden changes	(Kenneth et al. 2018)

2.4.3 Other Methods

Dai and Van Deusen (1996) developed a computer program based on statistical and signal processing theory to automatically detect peaks and valleys from sensor signals obtained during live heavy truck and falling-weight deflectometer testing. Statistical analysis was applied to each signal to characterize its nature and improve the efficiency of detecting maxima and minima. Noise effects were mitigated using filtering techniques, including Fast Fourier Transform (FFT) and time-domain filtering. The procedure proved effective and was used to process pavement response data collected at MnROAD between 1993 and 1996.

Dong et al. (2018) employed fiber Bragg grating (FBG) sensors to develop a wireless sensing network for airport asphalt pavement. Given the complex natural environment and aircraft loading conditions, they applied a moving average filter and FFT-based filter to process the sensor signals and extract critical dynamic response information. As shown in Figure 2.8, Dong et al. (2018) categorized the signal into aircraft-induced dynamic responses, temperature-affected responses, and unavoidable noise. They emphasized the importance of accounting for temperature variations when processing sensor data.

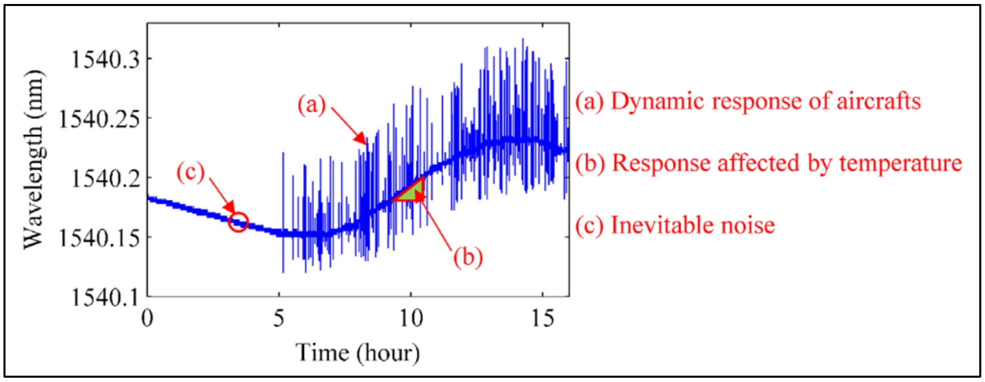

Figure 2.8 Raw monitoring data of a longitudinal sensor on a specific day. (Dong et al. 2018)

Concerned about the millions of data points generated during long-term monitoring, Manosalvas-Paredes et al. (2019) developed a data compression method for strain data measured by piezoelectric sensors. Instead of relying on single measurements (e.g., longitudinal strains), which are highly dependent on external conditions, the proposed approach focused on cumulative pavement responses. The innovation lay in utilizing the cumulative loading time of piezoelectric voltage as a reliable indicator of damage progression. Additionally, variations in activation times for threshold levels were identified as strong indicators of damage severity.

Dong et al. (2022) reviewed and discussed more than 40 data analysis methods used in pavement engineering. Among stochastic process methods, time series models—such as linear regression, moving averages, and exponential smoothing—were categorized under regression-based approaches for prediction. Dong et al. (2022) noted that time series modeling provides a straightforward means of forecasting future pavement performance based on historical data and has been widely applied to tasks such as smoothing pavement condition data, predicting rutting progression, and forecasting overall pavement performance.

Chapter 3: Data and Methodology

This chapter introduces the data collection methods and processing approaches used in the study. It begins with a description of the thermocouple sensors and their layout at MnROAD. Among the test cells examined, three are flexible pavements and two are rigid pavements. To address missing data from the thermocouples, a compressed sampling method is applied. Two spectral analysis techniques—Fourier Transform Analysis and Wavelet Analysis—are introduced. Additionally, a probabilistic analysis approach using the Monte Carlo Markov Chain (MCMC) method is presented.

All methods developed in this research were implemented in Python as an object-oriented package, facilitating code maintenance and integration with other platforms. The code is available through a GitHub repository and is accompanied by functional examples in a Jupyter notebook.

3.1 Weather Instrumentation and Data Collection

3.1.1 Thermocouple Sensors

In the MnROAD test sections, wired sensor technology was used to capture pavement temperatures. As shown in Figure 3.1, thermocouple (TC) sensors were constructed on site using Type T (copper-constantan) thermocouple extension cables to form a vertical thermocouple tree. TC sensors measure temperature through the junction of two dissimilar metal conductors, which generates a small voltage—known as the Seebeck voltage—proportional to the temperature difference between the hot junction and a reference junction.

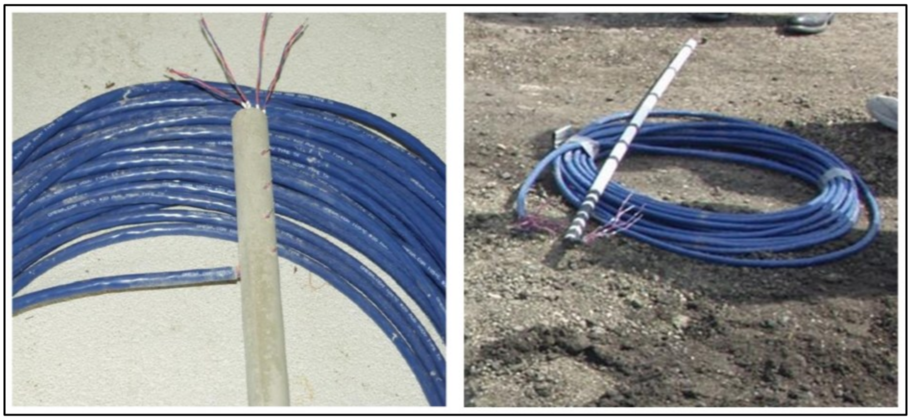

Figure 3.1 Thermocouple tree instrumentation (Podolsky et al. 2023)

3.1.2 Tested MnROAD Cells

Temperature data were collected from TC sensors embedded in five MnROAD test sections, including three flexible pavements and two rigid pavements. As shown in Figure 3.2, the MnROAD facility consists of two roadway segments running parallel to Interstate 94 near Otsego, Minnesota. The site includes a 3.5-mile mainline roadway that carries live interstate traffic and a 2.5-mile low-volume loop road where controlled truck weights and traffic volumes simulate rural road conditions. MnROAD features more than 50 test cells, each up to 500 feet in length, paved with varying thicknesses of concrete, asphalt, and aggregate. These cells are distributed across both roadways to represent a wide range of pavement types, with different combinations of surface, base, subbase, subgrade, drainage, and compaction conditions.

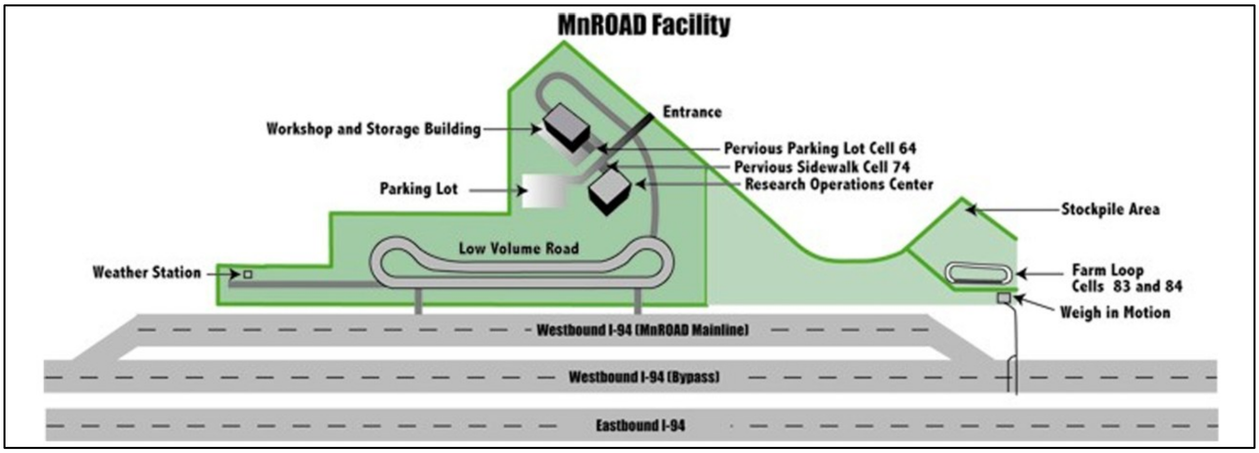

Figure 3.2 The MnROAD facility layout (Barnes, 2010)

As shown in Figures 3.3 and 3.4, TC sensor data were collected from cells 2, 3, 4, 12, and 13. Among these, cells 2, 3, and 4 are flexible pavements, while cells 12 and 13 are cement concrete pavements.

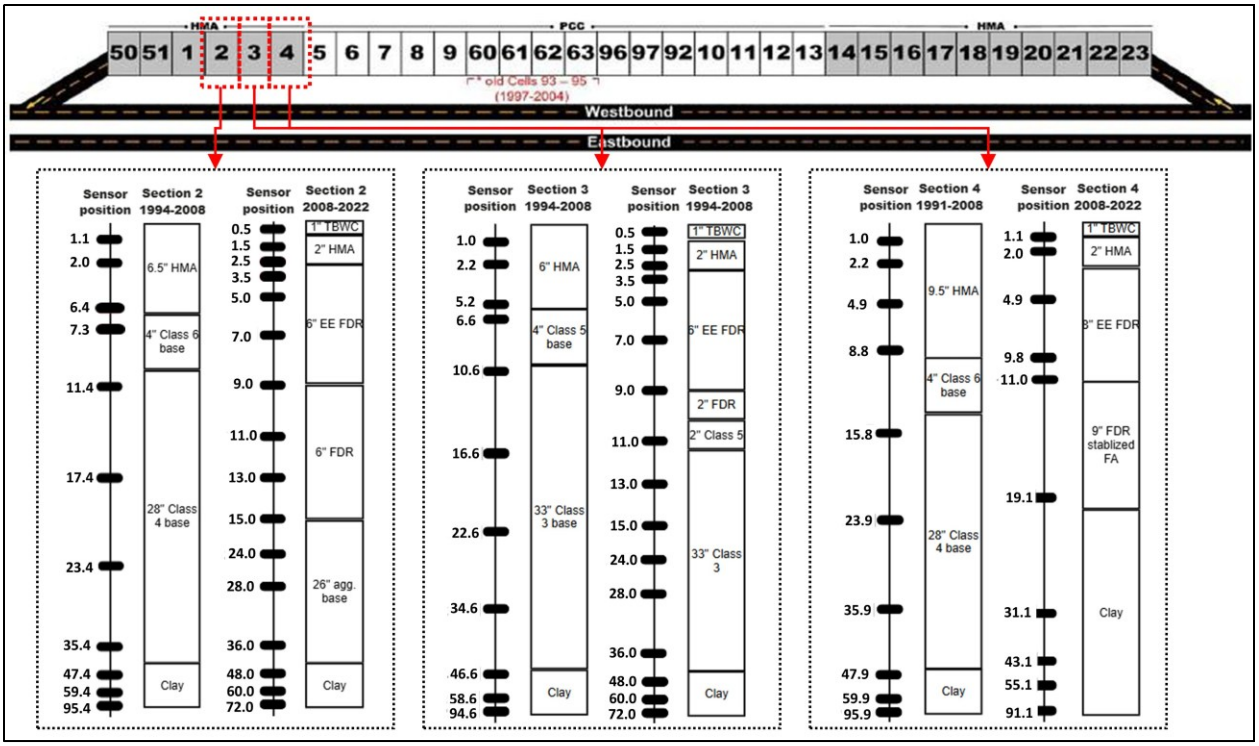

Figure 3.3 Cell layout, numbering, and pavement structure of flexible pavements

Cell 2 is 560 feet long and was constructed on a clay subgrade layer. Between 1994 and 2008, it consisted of 6.5 inches of hot mix asphalt over 4 inches of Class 6 base, which was placed on 28 inches of Class 4 base. After 2008, the cell was reconstructed on the same subgrade. The new structure consists of a 1-inch thin bonded wearing course (TBWC) over 2 inches of hot mix asphalt, on top of 6 inches of full-depth reclamation (FDR) stabilized with engineer emulsion (EE), over 6 inches of FDR, and finally 26 inches of aggregate base. Cell 3 is 454 feet long and was also constructed on a clay subgrade layer. Between 1994 and 2008, it consisted of 6 inches of hot mix asphalt over 4 inches of Class 5 base, on top of 33 inches of Class 3 base. After 2008, the cell was reconstructed on the same subgrade. The new structure consists of a 1-inch TBWC over 2 inches of hot mix asphalt, on 2 inches of FDR, 2 inches of Class 5 base, and 33 inches of Class 3 base. Cell 4 is 496 feet long and was constructed on a clay subgrade layer. Between 1991 and 2008, it consisted of 9.5 inches of hot mix asphalt over 4 inches of Class 6 base, on 28 inches of Class 4 base. After 2008, the cell was reconstructed on the same subgrade, with a structure consisting of a 1-inch TBWC over 2 inches of hot mix asphalt, on 9 inches of FDR stabilized with engineer emulsion (EE) and fly ash (FA).

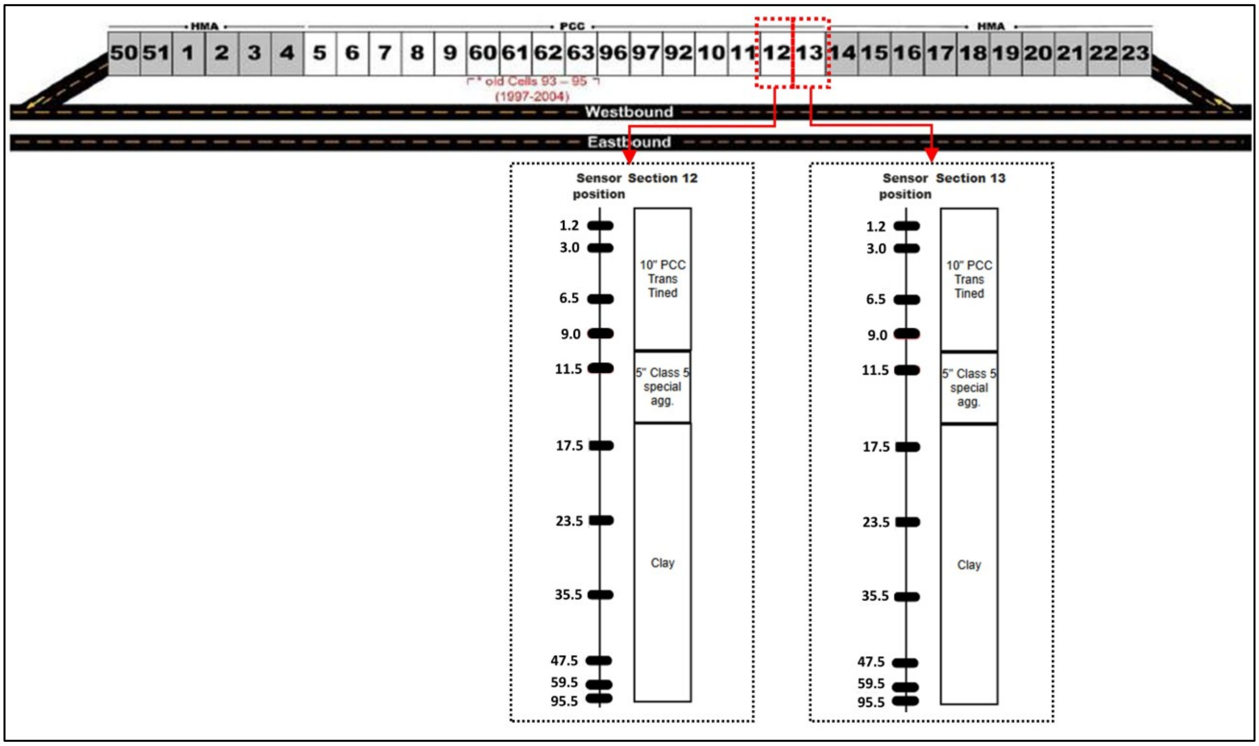

Figure 3.4 Cell layout, numbering, and pavement structure of rigid pavements

Cells 12 and 13 are each approximately 500 feet long and were constructed on a clay subgrade layer. Both cells have the same vertical structure: 10 inches of Portland Cement Concrete (PCC) over 5 inches of Class 5 special aggregate base, resting on the clay subgrade. The only difference between the two cells is the dowel size—cell 12 uses 1.25-inch diameter dowels, while cell 13 uses 1.5-inch diameter dowels. The panels in both test sections are 12 feet wide, but their lengths differ: cell 12 panels are 15 feet long, and cell 13 panels are 20 feet long. Another key difference is that cell 12 includes longitudinal edge drains at the shoulder joint adjacent to the driving lane, whereas cell 13 does not.

3.1.3 Weather Instrumentation

MnROAD has had weather stations since 1990, measuring weather conditions at both ends of the site. Data are collected every 15 minutes. In this research, air temperature (°C), relative humidity (%), and precipitation (cm) were used to relate to pavement system temperature data collected from the thermocouple sensors. This amounted to approximately 1.6 million weather data values. Weather data from the AWS, CRREL, and NW weather stations were used, covering the period from December 1, 1994, to November 16, 2007.

3.2 Data Treatment

The analysis developed in this research project required an extensive assessment of the common types of data corruption found in the datasets, and in the signals acquired with the thermocouple trees, the following types were identified:

- Noise
- Random missing data
- Random artifacts
- Long missing gaps
- Long train of artifacts

Noise is the most common type of data corruption in signal processing tasks, as illustrated in Figure 3.5a. It is inherent to data acquisition in experimental campaigns and cannot be reduced simply by adding more data to the dataset (Der Kiureghian &. Ditlevsen, 2009). Both the spectral and probabilistic methodologies developed in this research project are designed to handle this condition without requiring special treatment.

Next, sporadic missing data occurring at random time instants, as shown in Figure 3.5b, is also observed in the acquired signals. In this research, we found that a considerable portion of the signals was not acquired at a uniform sampling rate. Therefore, preprocessing is necessary to create a time-domain discretization with equal time increments Δt. Consequently, some entries of the acquired signal are assumed to be missing. To indicate these missing data points, we insert NaN (Not a Number) values, which will facilitate signal reconstruction at a later stage.

It is evident that a signal with missing data at random locations violates the Nyquist sampling theorem (Shannon, 1949), which states that any signal can be perfectly reconstructed from measured samples if the sampling rate is at least twice the highest frequency component of the signal. Since the maximum frequency of the sampled signal depends on the time increment Δt—which is non-uniform when data are missing at random locations—one cannot determine the exact sampling frequency. To overcome this challenge, techniques capable of recovering missing data under such conditions are needed. Compressed sampling (CS) (Candes, 2008) emerges as a powerful signal processing tool that leverages sparsity concepts for this purpose. However, when long gaps of signals are missing, the applicability of compressed sampling is limited, especially for reconstructing non-stationary signals, which is the focus of this research project.

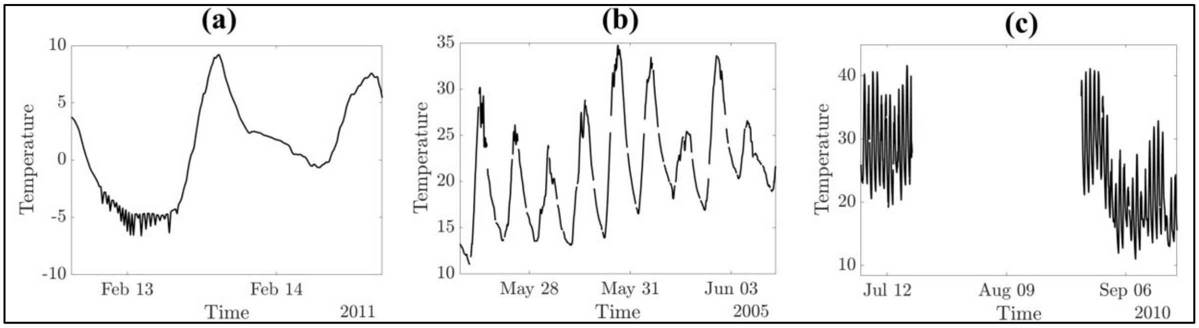

Figure 3.5 Temperature signal with a) noise, b) random missing data, and a c) long missing gap.

Artifacts are another common type of data corruption observed in the datasets used. Artifacts are characterized by localized disturbances in the signals and are typically represented as isolated spikes (see **Figure 3.6**a), though they can also appear as a train of spikes (**Figure 3.6**b). In **Figure 3.6**b, it is also evident that artifacts may be interspersed with missing data, which makes reconstruction in that region of the time series challenging, if not impossible. Therefore, this research project proposes a methodology to identify regions of each time series that are suitable for reconstruction using compressed sampling, aiming to enable their effective use in both spectral and probabilistic analyses.

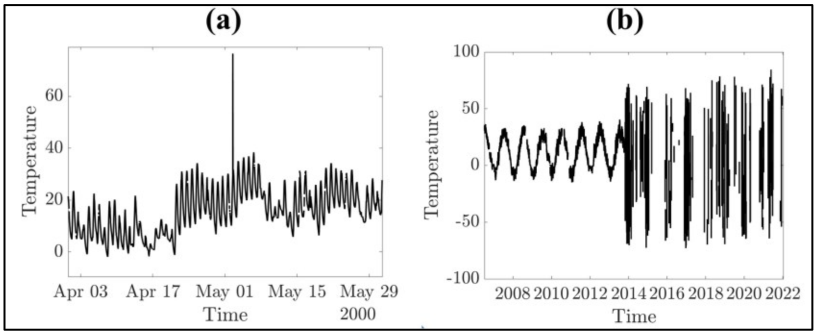

Figure 3.6 Temperature signal with a prominent a) artifact (spike) and a b) of artifacts (spikes).

3.2.1 Data segmentation and artifact removal

The collected data was reformatted and cleaned of artifacts to prepare it for analysis. Numerous instances of missing entries and inconsistent collection intervals necessitated imposing a fixed 15-minute time series across all sensor data. This normalization ensured a consistent temporal framework essential for subsequent analysis. In addition to correcting irregular time intervals and filling gaps, data artifacts—sensor readings identified as extreme outliers—were removed to improve data quality. Artifact removal was performed using the interquartile range (IQR) method for each sensor's dataset. Specifically, for each temperature time series, the first and third quartiles (Q1 and Q3) were calculated, and any data points outside the range $[Q1 - 1.5(IQR), Q3 + 1.5(IQR)]$ were excluded. All data points removed as artifacts, along with originally missing entries, were later reconstructed using the methods described in Section 3.2.2.

After generating an equally spaced, time-normalized dataset, it is crucial to assess data quality to enhance the accuracy of the reconstruction process. The primary goal at this stage is to identify and exclude segments where reconstruction is impossible—such as those heavily affected by sensor malfunctions, extreme noise, or prolonged data gaps. While conventional artifact removal techniques effectively handle datasets with few outliers, they often fail when corrupted or noisy data is prevalent. In such challenging scenarios, a more robust framework is required to manage these worst-case data conditions effectively.

The data quality assessment process involves the following steps:

1. Read the equally spaced signal.
2. Segment the data into overlapping time windows w_i of one year for each sensor, with a six-month overlap between consecutive windows.
3. Within each window w_i, model the temperature signal using a sine function of the form: $T(t) = Asin(\omega t + \phi) + D$, where the parameters to be optimized are: amplitude (A), frequency (ω), phase (ϕ), and a constant offset (D).
4. Predict the temperatures for the next six months using the optimized sine function.
5. Evaluate the prediction quality by computing the Mean Square Error (MSE), coefficient of determination (R^2), and the Frobenius norm ($||A_F||$).
6. Set acceptable thresholds for MSE, R^2, and $||A_F||$.
7. Filter the equally spaced dataset by applying the thresholds and excluding windows that do not meet all three criteria.
8. Recover the periods considered to contain healthy data based on the filtering results.

Numerical experiments showed that the following thresholds yield reliable results: MSE ≤ 50, $R^2 \geq 0.78$, and $||A_F|| \leq 1400$. Figure 3.7 illustrates step 6, showing the fitted sine function alongside the measured temperatures over a one-year period. It is evident that the predicted temperatures closely capture the mean behavior of the measured data.

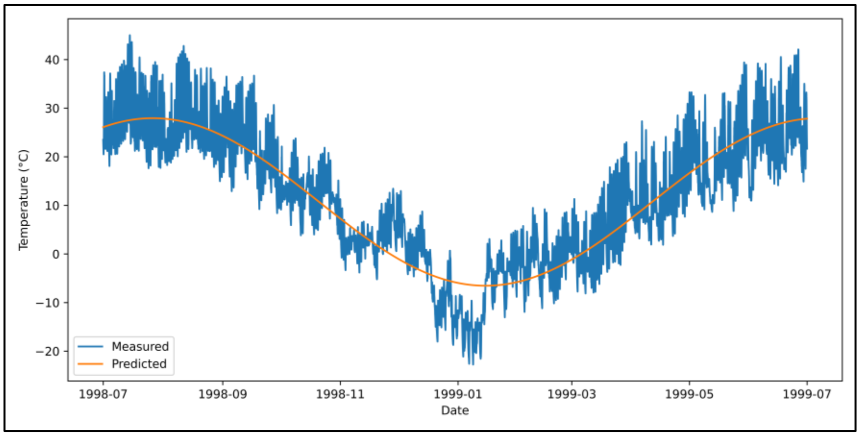

Figure 3.7 The predicted and measured temperatures.

In addition, Figure 3.8 shows the result of the proposed filtering algorithm applied to Thermocouple 12, Sensor 41. This sensor was selected because the latter portion of its measured temperature time series is clearly dominated by noise, likely due to sensor malfunction or environmental interference. After applying the filtering process, the algorithm successfully isolates the healthy portion of the signal, which is retained for use in the subsequent data reconstruction procedure.

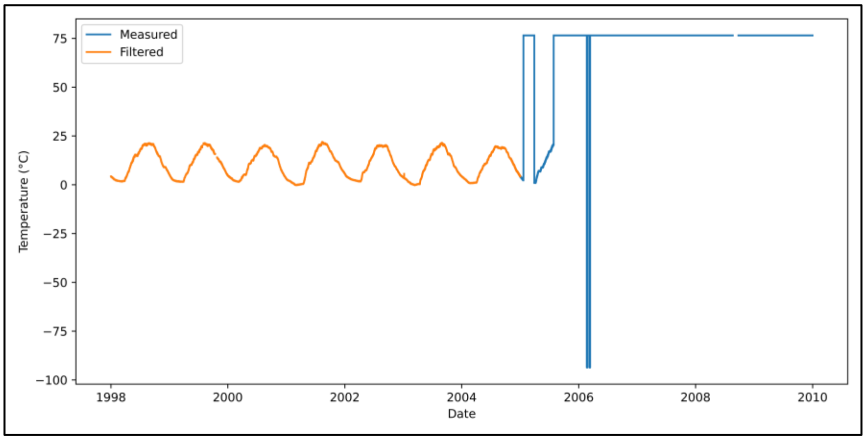

Figure 3.8 The predicted and filtered temperatures.

3.2.2 Data reconstruction

Missing data can be attributed to factors such as sensor failure during long-term data acquisition campaigns, which may result from environmental conditions, power outages, or maintenance activities. In this task, the team developed an algorithm for recover random missing data in the measured temperatures. To this end, CS was employed. In the figure below, we observe that a time-history—such as the temperature measured by thermocouple trees—also has a representation in the frequency domain. This frequency representation is obtained through integral transformations, such as the Fourier and wavelet transforms.

Signals with well-defined central frequencies, such as the temperature data used in this research project, are classified as narrowband and exhibit a sparse representation in the frequency domain. They are considered sparse because most of the signal's power is concentrated within very narrow frequency bands. As illustrated at the top of Figure 3.9, the signal is not sparse in the time domain, but its power is concentrated in a few large spikes in the frequency domain—indicating sparsity in that domain.

However, in practical applications, acquired signals are often corrupted by noise, and some data entries may be missing. When the noise magnitude is low, it typically appears as small, distributed spikes across the frequency domain (as shown at the top of Figure 3.9). But when the noise magnitude is high relative to the power of the underlying signal, the distinction between the signal and noise diminishes, and the sparse representation in the frequency domain is lost. In such cases, the spikes associated with the signal become indiscernible from those caused by noise. Therefore, the intensity of noise plays a critical role in the success of signal reconstruction.

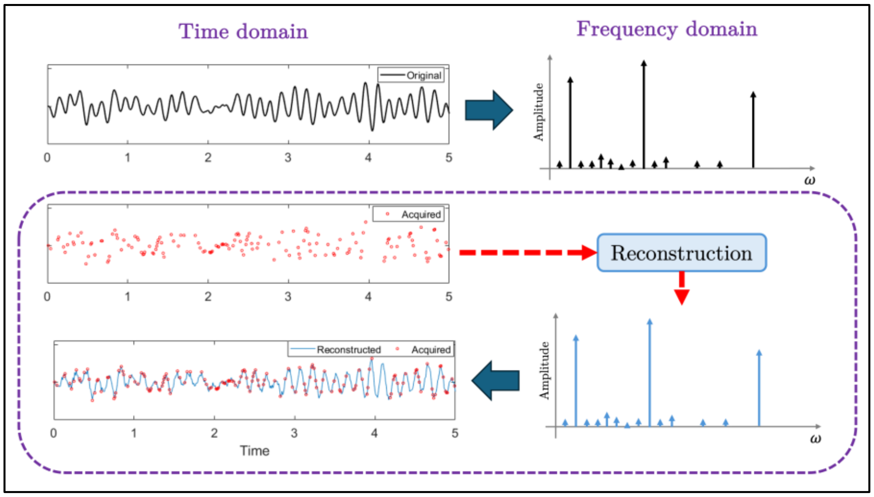

Figure 3.9 Representation of a complete signal in the time and frequency domains, its measured version contained missing data, and its reconstruction using its sparsity in the frequency domain.

Constructing the power spectrum from signals with missing data is generally prohibitive because it violates the Shannon–Nyquist sampling theorem. However, under appropriate assumptions, it is possible to recover the missing data with high probability when the signal is k-sparse—meaning its projection onto a basis that is incoherent with the observation space (e.g., Fourier or Generalized Harmonic Wavelet (GHW) bases) contains only k non-zero coefficients—and when the Restricted Isometry Property (RIP) holds. These are the two main principles of CS, also known as compressive sampling theory (Candes, 2008).

Since the temperature data were acquired over several years (e.g., 10 years), the resulting signals are very long. Consequently, representing them as an expansion over a basis of oscillating functions—such as the Fourier or wavelet basis—is computationally intensive due to the memory required to store the basis matrix, whose number of rows and columns is equal to the length of the acquired signal.

Let us assume that the acquired signal from each sensor in the thermocouple tree is denoted as $T_i^{(j)} = T^{(j)}(t_i)$, where j is the index of the sensor in the thermocouple tree and i is the index of the time instant such that time t is discretized as $[t_1, t_2, \ldots, t_N]$, with uniform spacing $t_{i+1} - t_i = \Delta t = 900s$. Thus, each signal $T_i^{(j)}$ can be represented as a column vector. In the approach developed in this research project, we assume that the real signal $T^{(j)}(t)$, which is continuous in the time domain, is acquired in a sampled form by the sensors. However, it is not uncommon that this signal is acquired with several missing data, which is represented in Figure 3.10 as the red dots.

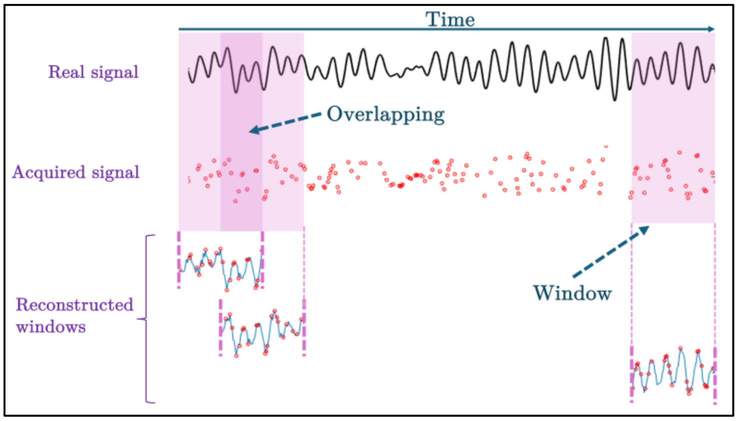

Figure 3.10 Recovery of missing data based on a rolling window strategy.

To reduce memory usage during the recovery of missing data in the signals acquired by each sensor in a thermocouple tree, we employed a windowing strategy. This strategy involves using a rolling window with 50% overlap to extract segments of the signal. Compressed sampling is then applied to each segment, which reduces computational cost while ensuring continuity in the reconstructed signal. Therefore, with the rolling window approach, we can extract the segment $T_l^{(j)} = [T_l^{(j)}, T_{l+1}^{(j)}, \ldots, T_{l+w}^{(j)}]$ of the signal $T^{(j)} = [T_1^{(j)}, T_2^{(j)}, \ldots, T_N^{(j)}]$, where w is the length of the window starting at the index l of the vector of time.

In this methodology, we assume that the column vector $T_l^{(j)}$ is acquired with a fixed sampling rate of 1 sample at each 900 s (15 minutes). Therefore, if any entry $T_i^{(j)}$ of this vector is missing, its value is represented as a NaN, as shown in Figure 3.11. Next, we employ CS to recover the missing data at each segment.

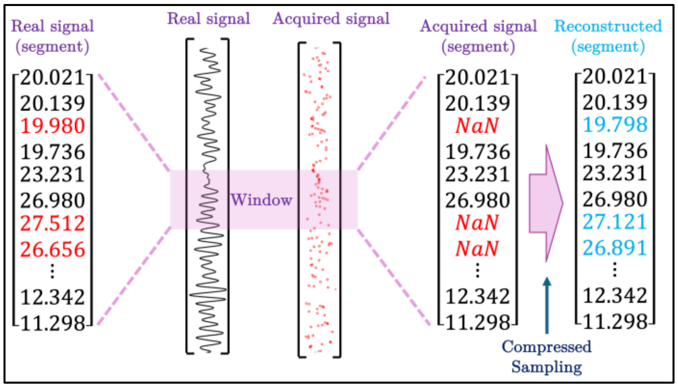

Figure 3.11 Numeric representation of a signal with missing data.

3.2.2.1 Compressed sampling

In CS, we assume that the signal $T_l^{(j)}$ with length w is sparse either in the frequency or in the joint time-frequency domain. By assuming that the signal is acquired with a uniform sampling rate, a projection of $T_l^{(j)}$ on a basis represented by the $w \times w$ matrix $\boldsymbol{B}$ is obtained by solving the linear system $T_l^{(j)} = \boldsymbol{B}x$ (see Figure 3.12) to obtain the vector of coefficients x with length w, which is in fact the representation $T_l^{(j)}$ either in the frequency or in the joint time-frequency domain.

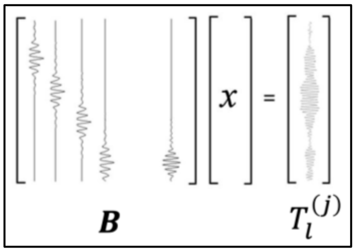

Figure 3.12 Projection of the temperature measurement onto an orthonormal basis.

However, when $T_l^{(j)}$ has missing data, we can remove the corresponding NaNs, such that the vector of measured data $\bar{T}_l^{(j)}$ has length $w - M$, where M is the number of missing data, as we observe in Fig. 3.13. Thus, to obtain a consistent linear system $\bar{T}_l^{(j)} = \bar{\boldsymbol{B}}x$, the $(w - M) \times w$ matrix $\bar{\boldsymbol{B}}$ is constructed by removing the rows at the same locations of the M missing data in $T_l^{(j)}$ (see Figure 3.13).

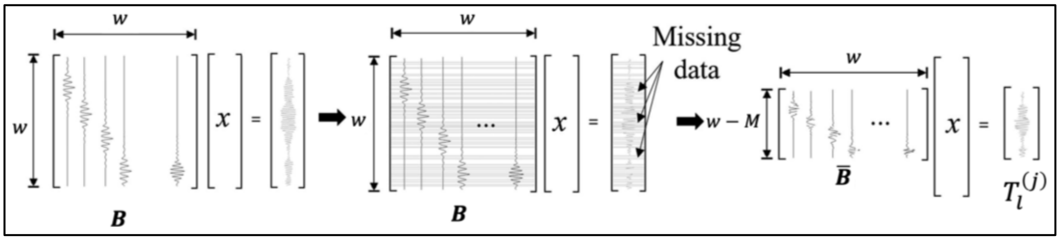

Figure 3.13 Construction of an indeterminate linear system of equations to be solved with CS.

Consequently, the linear system of equation $\overline{T}_l^{(j)} = \overline{\boldsymbol{B}}x$ becomes indeterminate, and it possess infinite solutions x. One of the solutions is obtained by solving it in the l_2-norm sense via least squares, such that:

$$x_{l_2} = \min\|x\|_{l_2} = \left[\overline{\boldsymbol{B}}^{T}\left(\overline{\boldsymbol{B}}\overline{\boldsymbol{B}}^{\boldsymbol{T}}\right)^{-1}\right]\overline{T}_l^{(j)} \tag{1}$$

where the term in the brackets is also known as pseudo-inverse of $\overline{\boldsymbol{B}}$. However, the theory of compressed sampling demonstrates that this is not the sparser solution. Therefore, could produce a noisy reconstruction $T_l^{(j)} = \boldsymbol{B}x_{l_2}$. In fact, the sparser solution is achieved by solving the linear system of equations in the l_0-norm sense, where the pseudo-norm l_0 return the number of non-zero entries in the vector. However, solving the norm minimization problem using the l_0-norm is computationally intractable because it becomes a combinatorial problem. Therefore, the requirement of sparsity is relaxed to include the norm l_1, which return the sum of the absolute values of the entries of a vector, which could serve as a proxy for the l_0-norm. In fact, the theory of compressed sampling demonstrates that under mild conditions, the sparser solution the linear system $T_l^{(j)} = \boldsymbol{B}x$ can be obtained in the l_1-norm sense. Therefore, the solution x_{l_1} is obtained by solving the following unconstrained optimization problem:

$$x_{l_1} = \min\left[\|x\|_{l_1} + \lambda\left\|\overline{T}_l^{(j)} - \overline{\boldsymbol{B}}x\right\|_{l_2}\right] \tag{2}$$

where λ is a regularization variable. This problem is also known as Lasso (least absolute shrinkage and selection operator) (Tibshirani, 1996).

Two examples of recovered signals are presented next. First, we can see in Figure 3.14 a segment of the data acquired with the first sensor in the thermocouple tree installed in cell 13. In Figure 3.15, we observe a closer look at a segment of the signal acquired by the first sensor of thermocouple 1 installed in cell 2. In both cases, we observe that CS can reliably recover the missing data in the acquired time series, while preserving the more significant spectral contents.

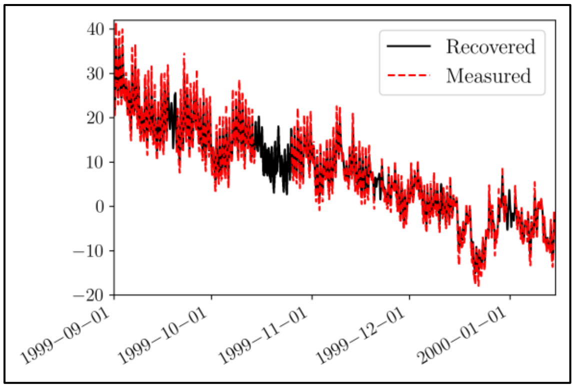

Figure 3.14 Segment of the signals acquired with the first sensor of the thermocouple tree in cell 13.

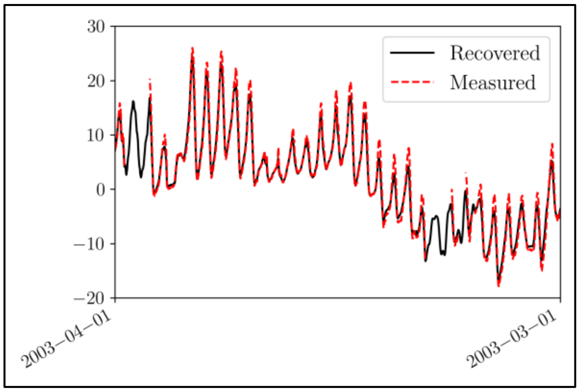

Figure 3.15 Segment of the signals acquired with the first sensor of the thermocouple tree 1 in cell 2.

3.3 Data Analysis

In this research project, we found that accurately determining the time-dependent behavior of the thermal properties of both rigid and flexible pavements requires advanced data analysis techniques. These are essential for efficiently interpreting the relationship between temperature fluctuations and pavement performance. Furthermore, the dynamic behavior of the temperature field in both spatial and temporal domains contains rich information about slowly varying and/or transient thermal phenomena. These are often linked to changes in pavement properties and environmental interactions, including extreme events such as heat waves and severe precipitation.

Thus, a comprehensive understanding of the temperature field's behavior across space and time is crucial for developing advanced and cost-effective pavement sensing methodologies based on temperature data. To address this need, we proposed two innovative approaches—one spectral and one probabilistic—for analyzing the relationship between pavement life-cycle performance and temperature dynamics. These methods are based on temperature measurements from thermocouple trees installed at five MnROAD test sections. In the following section, we present a comprehensive summary of the developed techniques for effectively modeling and analyzing both rigid (Sections 12 and 13) and flexible (Sections 2, 3, and 4) pavements.

3.3.1 Spectral Analysis

In this project, the time-varying behavior of pavement temperature is characterized by its daily and yearly fluctuations. In this project, we can focus on the spectral properties of the daily temperature fluctuations along the pavement depth. This allows us to identify time-localized properties of a mathematical model representing the pavement system. Determining these localized properties facilitates the analysis of their evolution on a coarser time scale. Consequently, it becomes possible to track how these properties change over the years with high accuracy.

3.3.1.1 Filter modeling

In this project, we model temperature fluctuations as time histories that are filtered by the pavement layers along their depth (see Figure 3.16). This interpretation enables the development of methodologies for analyzing key properties—such as the gain and phase shift—of a filter that represents the dynamic behavior of temperature fluctuations between two distinct layers of the pavement structure. These properties serve as indicators of slow, time-dependent changes in the thermal characteristics of the materials, which may result from processes such as degradation, densification, or localized anomalies caused by extreme events like severe precipitation.

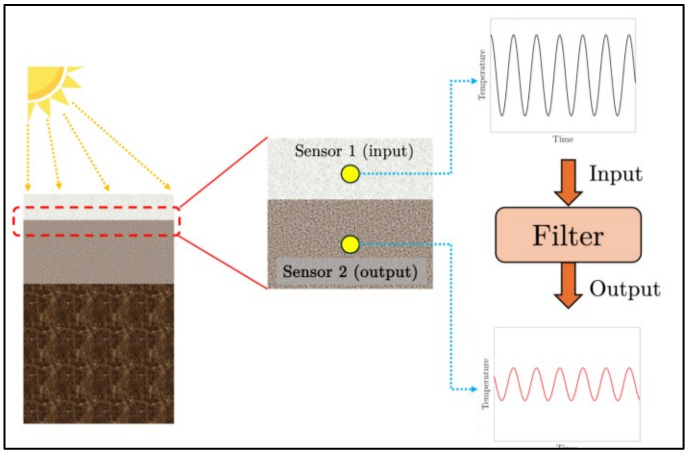

Figure 3.16 Measurement from adjacent sensors used to model a filter encoding the dynamics of the thermal properties of pavements.

Any system that produces an output time history in response to an input signal can be mathematically modeled as a filter—either in the frequency domain, assuming the system is time-invariant, or in the joint time-frequency domain, assuming the system is time-variant. In this context, the time-varying behavior of the system is primarily characterized by changes in the spectral content of both the input and output signals.

In this project, we model the pavement as a cascade of filters (see Figure 3.17), where spectral properties such as gain and phase are largely determined by the thermal properties of the medium. Specifically, the state of each filter in the cascade corresponds to the properties of the material between two consecutive sensors in a thermocouple tree. Since the first sensor is embedded in the surface layer, other heat transfer mechanisms—such as convection or albedo—are not considered.

Given that heat conduction governs the filter behavior, we can identify the filter characteristics in both the frequency, and joint time-frequency domains based on temperature readings from the thermocouple sensors. The identified filter state thus serves as a time-varying indicator of the thermal properties of the pavement layers. This, in turn, provides insight into pavement condition, as changes in thermal conductivity are closely linked to material aging, structural damage, and exposure to extreme environmental conditions.

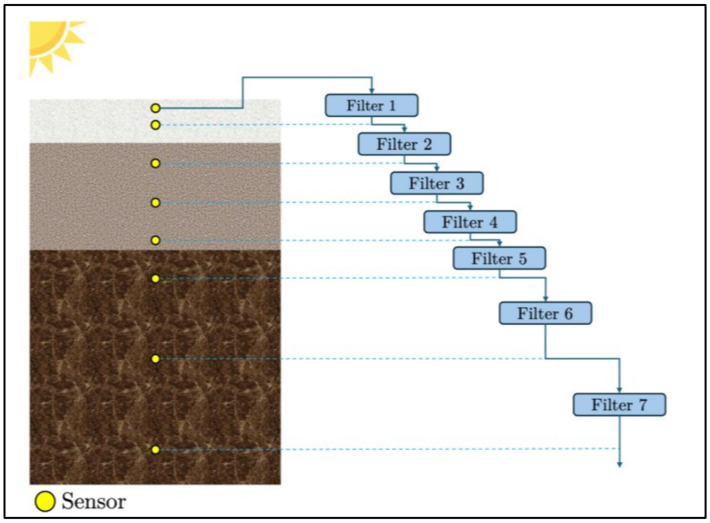

Figure 3.17 Filter cascade used to model multiple segments of the pavement structure.

In the proposed filter modeling and identification through an appropriate spectral analysis, we assume that the temperature fluctuations at a given sensor j are represented as a time-history $T^{(j)}(t)$ with components at several frequencies. As the temperature fluctuates with well-defined daily and yearly periods, we can easily determine the central frequencies of the spectral components with most prominent power. To this end, we first determine the sampling rate of the signals acquired by the sensors installed at the thermocouple trees. In this regard, the time interval between measurements is equal to 15 mins, which gives a sampling period equal to 900 s. Furthermore, one day has a period equal to 86,400 s, which means that the main frequency of daily fluctuations is equal to $1.157 \times 10^{-5} Hz$. Moreover, the temperature fluctuations in a year have a frequency equal to $3.1688 \times 10^{-8} Hz$. As we observe, the frequencies of both daily and yearly fluctuations are very low, but the fact that they are well-defined is relevant for performing the filter modeling and identification.

To construct the proposed methodology, we focus on two adjacent sensors (see Fig. 3.17), where the input $T^{(j)}(t)$ and output $T^{(j+1)}(t)$ signals, corresponding to sensors j and $j+1$, respectively, are represented in a discretized form as the time-series $T_i^{(j)} = T^{(j)}(t_i)$ and $T_i^{(j+1)} = T^{(j+1)}(t_i)$, where the time t is discretized as $[t_1, t_2, \ldots, t_N]$, where $t_{i+1} - t_i = \Delta t = 900s$. In this regard, the signals after an appropriate data treatment, have a length equal to N, such that it covers a long period $t_f = (N-1)\Delta t$ of the pavement life-cycle.

Next, using both input $T_i^{(j)}$ and output $T_i^{(j+1)}$ signals, we can proceed with the determination of the frequency response function $H(\omega)$ (or $H(\omega, t)$ for a time-variant filter) of an hypothetical black-box system modeled as a filter, and whose gain and phase shift will be associated with the thermal performance of the layers of the pavement with respect to heat conduction.

The primary objective of analyzing the properties of the identified filter as a proxy for pavement performance lies in its sensitivity to both abrupt and gradual changes in the pavement's thermal properties. These changes are associated with short-term extreme events—such as heat waves and severe precipitation—as well as long-term processes like aging and damage accumulation throughout the pavement's life cycle. Additionally, the filter model captures the natural evolution of material properties over time, such as densification.

The following sections present a summary of the two techniques developed for this analysis. The first technique is based on the Fourier transform and assumes that the signal is stationary within predefined time intervals. It produces a time-independent filter for each interval. The second technique uses wavelet analysis and employs a specialized wavelet known as the Generalized Harmonic Wavelet (GHW), which eliminates the need to assume stationarity over fixed intervals. Furthermore, GHW enables spectral analysis over fixed frequency bandwidths—something not feasible with conventional wavelets such as the Morlet wavelet.

3.3.1.2 Fourier Transform Analysis

The Fourier transform is employed in signal processing to map signals from the time and frequency domains. In this regard, we use this approach to determine the FRF $H(\omega)$ of a linear time-invariant system (LTI) modeling the relation between the signals of two adjacent sensors in the thermocouple tree, as described in the previous section. To this end, we assume that the filter is a black-box that receives the input signal $T_i^{(j)}$ and "produces" the signal $T_i^{(j+1)}$ as an output, which corresponds to the temperature read by the sensor $j+1$ at a position right below the sensor j.

The Fourier transform and its inverse are given by the following expressions (Oppenheim et al., 1996):

$$T^{(j)}(\omega) = \int_{-\infty}^{\infty} T^{(j)}(t) e^{-\hat{\jmath}\omega t} dt \tag{3}$$

$$T^{(j)}(t) = \int_{-\infty}^{\infty} T^{(j)}(\omega) e^{\hat{\jmath}\omega t} d\omega \tag{4}$$

where $\hat{\jmath} = \sqrt{-1}$. The Fourier transform is necessary to determine a representation of the signal in the frequency domain. However, to determine $H(\omega)$, we need to find how the power of each signal component is distributed in the frequency domain. To this end, the auto- and cross- power spectra of the input and output signals must be determined.

In this methodology, the input $T_i^{(j)}$ and output $T_i^{(j+1)}$ signals cover a long period t_f of the pavement life-cycle (e.g., 10 years). Therefore, as we are interested in determining how the properties of the filter changes over time, we divide the signal with length N into k smaller sub-intervals of length N_k, which could correspond, for example, to a period of 14 days (e.g., $N_k = 12{,}600$). Thus, for each sub-interval, we determine the auto power spectrum $S_{T^{(j)}T^{(j)}}(\omega)$ of the input signals $T_{k,i}^{(j)}$, the auto-power spectrum $S_{T^{(j+1)}T^{(j+1)}}(\omega)$ of the output signal $T_{k,i}^{(j+1)}$, and the cross-power spectrum $S_{T^{(j+1)}T^{(j)}}(\omega)$ for both input and output signals, are given by the following expressions:

$$S_{T^{(j)}T^{(j)}}(\omega) = \frac{\mathbb{E}\left[T^{(j)}(\omega)\bar{T}^{(j)}(\omega)\right]}{N_k\,\Delta\omega} \tag{5}$$

$$S_{T^{(j+1)}T^{(j+1)}}(\omega) = \frac{\mathbb{E}\left[T^{(j+1)}(\omega)\bar{T}^{(j+1)}(\omega)\right]}{N_k\,\Delta\omega} \tag{6}$$

$$S_{T^{(j+1)}T^{(j)}}(\omega) = \frac{\mathbb{E}\left[T^{(j+1)}(\omega)\bar{T}^{(j)}(\omega)\right]}{N_k\,\Delta\omega} \tag{7}$$

respectively, where $\bar{T}$ is the complex conjugate of T and $\mathbb{E}[\cdot]$ is the expectation operator, which is employed as a smoothening operator. Therefore, with the estimated power spectra, we can proceed with the determination of the LTI-FRF and the coherence, which serve as an indicator of the modeling error, providing information about the "goodness-of-fit" of the model subject to the measured data. A coherence close to one, means that the linear model is valid; otherwise, if the coherence gets close to zero, the linear model is not reliable enough.

The LTI-FRF is given by the expression

$$H_k^{(j,j+1)}(\omega) = \frac{S_{T^{(j+1)}T^{(j)}}(\omega)}{S_{T^{(j)}T^{(j)}}(\omega)} \tag{8}$$

and the coherence is given by

$$\left(\gamma_k^{(j,j+1)}\right)^2(\omega) = \frac{\left|S_{T^{(j+1)}T^{(j)}}(\omega)\right|^2}{S_{T^{(j+1)}T^{(j+1)}}(\omega)S_{T^{(j)}T^{(j)}}(\omega)} \tag{9}$$

Thus, as the LTI-FRF is complex-valued, we can determine the filter gain $A_k^{(j,j+1)}(\omega)$ and phase shift $\phi_k^{(j,j+1)}(\omega)$ as follows:

$$\phi_k^{(j,j+1)}(\omega) = \operatorname{atan}\left[\frac{\operatorname{Im}\left(H_k^{(j,j+1)}(\omega)\right)}{\operatorname{Re}\left(H_k^{(j,j+1)}(\omega)\right)}\right] \tag{10}$$

$$A_k^{(j,j+1)}(\omega) = \left|H_k^{(j,j+1)}(\omega)\right|^2 \tag{11}$$

where $\mathrm{Im}(\cdot)$ and $\mathrm{Re}(\cdot)$ are the imaginary and real parts of a complex number. Therefore, with this approach we can have a coarse representation of the time-dependent behavior, as determined by the sub-interval k, of both phase $\phi_k^{(j,j+1)}(\omega)$ and gain $A_k^{(j,j+1)}(\omega)$.

The mechanization of the proposed Fourier analysis is outlined below:

1. Select two adjacent sensors in the thermocouple tree, such as at the interface between two layers of the pavement structure.
2. Determine the time discretization such that $t_i = (i-1)\Delta t$ and $t = [t_1, t_2, \dots, t_N]$.
3. Consider that the first sensor is above the second one and assume that the input signal is the temperature measured by the first sensor and the output signal is the temperature measured in the second sensor, such that $T_i^{(j)}$ corresponds to the temperature measured by the sensor j at the time instant t_i.
4. Divide the time histories $T^{(j)}$ and $T^{(j+1)}$ of length N of sensors j and $j+1$ into k sub-intervals.
5. For each sub-interval k, compute $H_k^{(j,j+1)}(\omega)$ and $\left(\gamma_k^{(j,j+1)}\right)^2(\omega)$.
6. If for the central frequency ($f_d = 1.157 \times 10^{-5} Hz$) of the daily fluctuation $\left(\gamma_k^{(j,j+1)}\right)^2(\omega) > 0.5$, accept the linear model and compute $\phi_k\left(\frac{f_d}{2\pi}\right)$ and $A_k\left(\frac{f_d}{2\pi}\right)$.
7. Use $\phi_k\left(\frac{f_d}{2\pi}\right)$ and $A_k\left(\frac{f_d}{2\pi}\right)$ to infer about the time evolution of these parameters to track the ageing of the pavement.

3.3.1.3 Wavelet Analysis

One of the main limitations of using the Fourier transform to analyze naturally time-variant systems is the assumption that the signal remains stationary within a sub-interval k of the time domain. As a result, this technique fails to accurately localize transient thermal phenomena—such as those associated with severe weather events—because it relies on estimating the average signal power within each sub-interval, thereby smoothing out short-lived events.

To address the spectral estimation of non-stationary time series, several techniques have been developed, including traditional methods like the Short-Time Fourier Transform (STFT) (Allen and Rabiner, 1977) and the Wigner–Ville Distribution (WVD) (Ville, 1948). However, STFT suffers from limited time-frequency localization due to the uncertainty principle inherent in the Fourier transform, which particularly hinders its ability to analyze low-frequency components. Meanwhile, the performance of the Wigner–Ville Distribution deteriorates when applied to multi-component or nonlinear frequency-modulated mono-component signals (Pachori and Nishad, 2016).

As an alternative, wavelets have been widely used in multiresolution analysis of signals in the joint time-frequency domain. Wavelets constitute a family of orthogonal functions that offer strong localization properties in both time and frequency domains. The concept of wavelets was originally introduced by Morlet for geophysical data analysis, and a rigorous mathematical foundation was later developed in the field of harmonic analysis (Daubechies, 1992), focusing on the representation of square-integrable functions—such as continuous-time signals—in terms of an orthonormal basis in Hilbert space.

To overcome the limitations, we propose using a special class of wavelets known as Generalized Harmonic Wavelets (GHW) to identify a linear time-variant filter capable of capturing the non-stationary behavior of both input and output signals. GHWs are defined by two scale parameters, m and n, which independently control the central frequency and bandwidth at each scale in the frequency domain, and a parameter kk that controls the wavelet's time localization. A significant advantage of GHWs is their ability to provide enhanced frequency localization—particularly at low frequencies—thanks to the decoupling of scale parameters from the central frequency. This is not typically possible with conventional wavelet families such as the Morlet wavelet (Morlet, 1982).

Unlike the dyadic partitioning of the time-frequency grid employed by standard wavelets (e.g., Morlet, 1982; Mallat, 1999), GHWs allow flexible and adaptive resolution tailored to the frequency range of interest, offering improved localization in the time-frequency domain (see Figure 3.18).

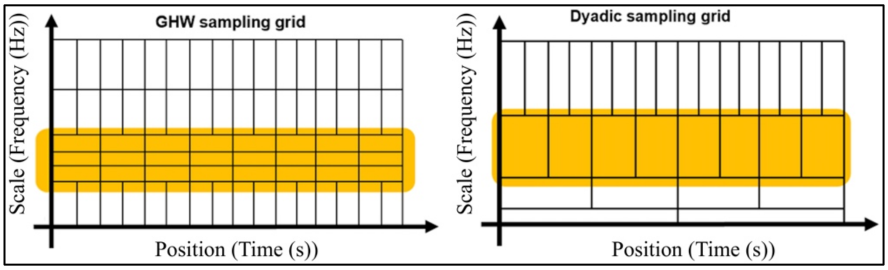

Figure 3.18 Wavelet-based joint time-frequency domain partition; GHW-based enhanced localized frequency resolution, compared with standard dyadic wavelet partition (Miller et al., 2020).

Additionally, GHWs feature a non-overlapping, box-shaped frequency spectrum, which provides favorable orthogonality properties for analytical and mathematical derivations (see Figure 3.19). Specifically, the scale (m, n) and time localization (k) determine a wavelet with bandwidth $m\Delta\omega \leq \omega < n\Delta\omega$ and with the following representation in the frequency domain:

$$\Psi^{G}_{(m,n),k}(\omega) = \begin{cases} \frac{1}{(m-n)\Delta\omega} e^{-\jmath\omega\frac{kT_0}{m-n}}, & \text{if } m\Delta\omega \leq \omega < n\Delta\omega \\ 0, & \text{otherwise} \end{cases} \tag{12}$$

where T_0 is the time length of the signal being analyzed, $\Delta\omega = 2\pi/T_0$.

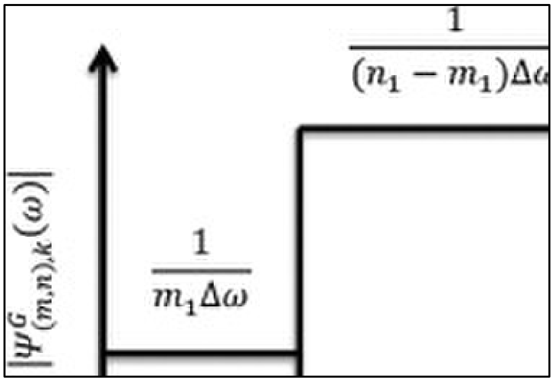

Figure 3.19 A generalized harmonic wavelets basis example spanning non-overlapping intervals of arbitrary bandwidths in the frequency domain (Kougioumtzoglou, 2013).

Therefore, the GHW transform of a signal $T^{(j)}(t)$ is given by (Newland, 1994)

$$\mathrm{W}^G_{(m,n),k}\left[T^{(j)}(t)\right] = \frac{n-m}{T_0}\int_{-\infty}^{\infty} \overline{IFT}\left[\Psi^G_{(m,n),k}(\omega)\right] T^{(j)}(t)dt \tag{13}$$

where $\overline{IFT}\left[\Psi^G_{(m,n),k}(\omega)\right]$ is the complex conjugate of the inverse Fourier transform of $\Psi^G_{(m,n),k}(\omega)$. Therefore, the Perseval's theorem (Oppenheim and Schaffer, 2010) combined with the non-overlapping characteristics of the wavelet ensure the estimation of the auto- and cross- spectra of the input and output signals in the joint time-frequency domain as follows:

$$S_{T^{(j)}T^{(j)}}(\omega, t) = S^{(j,j)}_{(m,n),k} = \frac{\mathbb{E}\left[\mathrm{W}^G_{(m,n),k}[T^{(j)}(t)]\overline{\mathrm{W}}^G_{(m,n),k}[T^{(j)}(t)]\right]}{(n-m)\Delta\omega} \tag{14}$$

$$S_{T^{(j+1)}T^{(j+1)}}(\omega, t) = S^{(j+1,j+1)}_{(m,n),k} = \frac{\mathbb{E}\left[\mathrm{W}^G_{(m,n),k}[T^{(j+1)}(t)]\overline{\mathrm{W}}^G_{(m,n),k}[T^{(j+1)}(t)]\right]}{(n-m)\,\Delta\omega} \tag{15}$$

$$S_{T^{(j+1)}T^{(j)}}(\omega, t) = S^{(j+1,j)}_{(m,n),k} = \frac{\mathbb{E}\left[\mathrm{W}^G_{(m,n),k}[T^{(j+1)}(t)]\overline{\mathrm{W}}^G_{(m,n),k}[T^{(j)}(t)]\right]}{(n-m)\,\Delta\omega} \tag{16}$$

where each wavelet is localized in $\frac{kT_0}{n-m} \le t < \frac{(k+1)T_0}{n-m}$. Therefore, we do not need to break the full time-histories into smaller segments to determine the time evolution of the FRF. In this regard, the LTV-FRF $H^{(j,j+1)}(\omega, t)$ is obtained in the joint time-frequency domain, which aids the estimation of time dependent phase shift $\phi^{(j,j+1)}(\omega, t)$ and gain $A^{(j,j+1)}(\omega, t)$. Furthermore, the localization characteristics of the GHW enables the determination of LTV-FRF $H^{(j,j+1)}_{(m,n),k}$, the phase shift $\phi^{(j,j+1)}_{(m,n),k}$, and gain $A^{(j,j+1)}_{(m,n),k}$ only at the scale of interest in the wavelet domain determined by the scale (m, n) and time localization (k). Therefore, the LTV-FRF in the GHW domain is given by the expression

$$H_{(m,n),k}^{(j,j+1)} = \frac{S_{(m,n),k}^{(j+1,j)}}{S_{(m,n),k}^{(j,j)}} \tag{17}$$

and the coherence is given by

$$\left(\gamma_{(m,n),k}^{(j,j+1)}\right)^2 = \frac{\left|\langle S_{(m,n),k}^{(j+1,j)}\rangle\right|^2}{\langle S_{(m,n),k}^{(j+1,j+1)}\rangle\langle S_{(m,n),k}^{(j,j)}\rangle} \tag{18}$$

where $\langle\cdot\rangle$ is a smoothing operator, for example a Gaussian filter. Thus, as the LTI-FRF is complex-valued, we can determine the filter gain $A_k(\omega)$ and phase shift $\phi_k(\omega)$ as follows:

$$\phi_{(m,n),k}^{(j,j+1)} = \text{atan}\left[\frac{\text{Im}\left(H_{(m,n),k}^{(j,j+1)}\right)}{\text{Re}\left(H_{(m,n),k}^{(j,j+1)}\right)}\right] \tag{19}$$

$$A_{(m,n),k}^{(j,j+1)} = \left|H_{(m,n),k}^{(j,j+1)}\right|^2 \tag{20}$$

where $\text{Im}(\cdot)$ and $\text{Re}(\cdot)$ are the imaginary and real parts of a complex number. Therefore, with this approach we can have a fine representation of the time-dependent behavior of both phase $\phi^{(j,j+1)}(\omega,t)$ and gain $A^{(j,j+1)}(\omega,t)$.

The mechanization of the proposed GHW analysis is outlined below:

1. Select two adjacent sensors in the thermocouple tree, such as at the interface between two layers of the pavement structure.
2. Determine the time discretization such that $t_i = (i-1)\Delta t$ and $t = [t_1, t_2, \ldots, t_N]$.
3. Consider that the first sensor is above the second one and assume that the input signal is the temperature measured by the first sensor and the output signal is the temperature measured in the second sensor, such that $T_i^{(j)}$ corresponds to the temperature measured by the sensor j at the time instant t_i.
4. Determine m and n such that the central frequency ($f_d = 1.157 \times 10^{-5} Hz$) of the daily fluctuation is the central frequency of the wavelet, which is given by $\frac{f_d}{2\pi} = \omega_d = \frac{n+m}{2}\Delta\omega$.
5. Compute the auto power spectra $S_{(m,n),k}^{(j,j)}$ and $S_{(m,n),k}^{(j+1,j+1)}$ of $T^{(j)}$ and $T^{(j+1)}$, respectively, as well as the cross power spectrum $S_{(m,n),k}^{(j+1,j)}$.
6. Compute $H_{(m,n),k}^{(j,j+1)}$ and $\left(\gamma_{(m,n),k}^{(j,j+1)}\right)^2$.

7. If for the central frequency $f_d \left(\gamma_{(m,n),k}^{(j,j+1)}\right)^2 > 0.5$, accept the linear model and compute $\phi_{(m,n),k}^{(j,j+1)}$ and $A_{(m,n),k}^{(j,j+1)}$.

Use $\phi_{(m,n),k}^{(j,j+1)}$ and $A_{(m,n),k}^{(j,j+1)}$ to infer about the time evolution of these parameters to track the ageing of the pavement.

3.3.2 Probabilistic Analysis

The objective of the probabilistic analysis in this study is twofold. First, we aim to validate the results obtained through spectral analysis. Second, we seek to develop an inverse analysis tool for estimating the thermal properties of pavement materials, which serve as a proxy for assessing pavement condition. Special emphasis is placed on characterizing the heat conduction mechanisms between adjacent pavement layers, as these interactions are directly influenced by the thermal diffusivity and conductivity of the constituent materials.

To this end, we model the heat transfer process in pavements using a simplified thermal conduction model based on the one-dimensional heat equation. This simplification is chosen to facilitate the use of Bayesian inference techniques, which allow for the estimation of thermal parameters from temperature measurements recorded across both space and time. The probabilistic framework provides a robust mechanism for quantifying uncertainties in the estimated parameters, especially in the presence of measurement noise and model imperfections.

In this research, we employed the Markov Chain Monte Carlo (MCMC) method, specifically using the Metropolis-Hastings algorithm, within a Bayesian inference framework to estimate the thermal diffusivity coefficient of pavement layers. The forward problem is governed by the heat equation, which describes the evolution of temperature in a thermally conducting medium. Observed temperature data from thermocouple arrays installed within the pavement structure were used to inform the inverse analysis.

Bayesian inference offers a principled approach to update prior knowledge about uncertain parameters based on empirical observations, resulting in a posterior probability distribution that incorporates both prior beliefs and measurement data. The inverse heat conduction problem (IHCP) is a classic example where such Bayesian approaches excel. It involves estimating unknown parameters—such as thermal diffusivity, thermal conductivity, boundary heat flux, or initial temperature distributions—from internal temperature measurements. MCMC methods are ideal for this task, as they generate samples from the posterior distribution, enabling not only parameter estimation but also credible interval computation. For example, Wang and Zabaras (2004) applied an MCMC framework with a Markov Random Field (MRF) prior to estimate boundary heat fluxes from interior temperature observations. Their forward model solved the heat equation under the assumption of additive white Gaussian noise in the measurements. Their results demonstrated high accuracy and effective uncertainty quantification in both 1D and 2D configurations. Similarly, Gnanasekaran and Balaji (2013) applied MCMC techniques to estimate the thermal diffusivity α in a controlled laboratory heat transfer experiment. They reported posterior estimates along with standard deviations, showcasing the strength of Bayesian methods in delivering parameter estimates with explicit uncertainty quantification—an essential feature for robust decision-making in engineering diagnostics.

3.3.2.1 Mathematical model: heat equation

The objective of this task is to find an appropriate mathematical model describing the dynamics of the heat conduction in pavements. To this end, we assume that a pavement is a heterogeneous medium whose thermal properties changes along in space and time. Therefore, since the sensors are embedded in the pavement structure, the physics of this problem is governed by the heat conduction expressed by the following equation:

$$\frac{\partial T(y,t)}{\partial t} = \alpha(y,t)\frac{\partial T^2(y,t)}{\partial y^2} \tag{21}$$

$$\text{with initial and boundary conditions} \begin{cases} T(y,0) = T_0(y) \\ T(0,t) = T^{(0)}(t) \\ T(L,t) = T^{(s)}(t) \end{cases}$$

where y is the depth, t is the time, $\alpha(y,t)$ is the thermal diffusivity, L is the distance between the first and the last sensor mounted in the thermocouple tree. Furthermore, we have assumed a unidimensional model with Dirichlet boundary conditions $T^{(0)}(t)$ and $T^{(s)}(t)$ and initial condition $T^{(0)}(t)$, because the thermocouple tree measures the temperature along a line through the pavement depth, as represented by the rod in Figure 3.20 for cell 12. In this figure, the sensors are the points along the depth where the temperature field is measured. Therefore, for a given thermocouple tree with s sensors, we have predetermined depths $y_j \in [y_1, y_2, \dots, y_s]$. Therefore, the measured temperature field is mathematically represented as $T_i^{(j)} = T(y_j, t_i)$, where the discretize vector of time is given by $t_i \in [t_1, t_2, \dots, t_N]$. Additionally, we have assumed that thermal diffusivity α is constant within each layer of the pavement, since we are assuming a homogeneous thermal characteristic for a layer composed by the same material. In the example shown in Figure 3.20, we observe that Cell 12 is composed with three layers, and therefore our rod model contains three sections made of materials with three distinct thermal diffusivities $\alpha_1(t)$, $\alpha_2(t)$, and $\alpha_3(t)$.

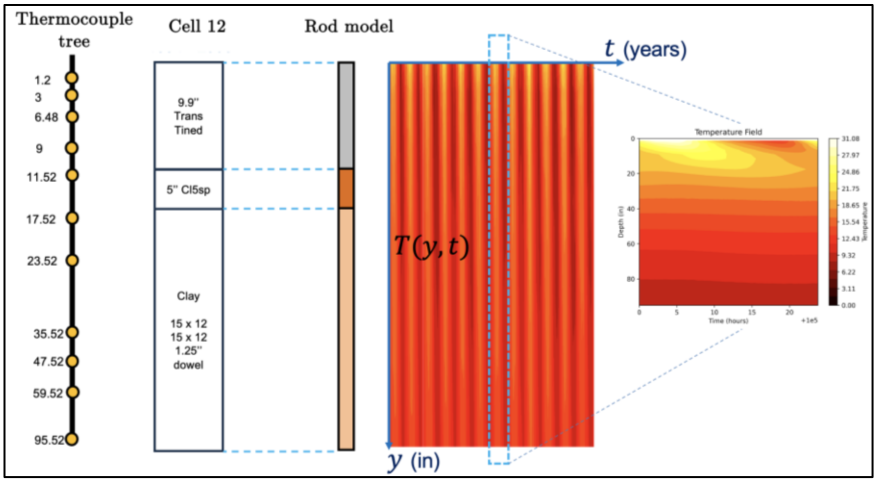

Figure 3.20 Model for the thermal conduction along the pavement depth.

However, determining time-dependent thermal diffusivities is a challenging task due to the complexity and ill-posed nature of the inverse problem. To reduce this complexity, we assume that changes in the thermal properties of the pavement occur gradually over time. Consequently, within a single day, the thermal diffusivity coefficients $\alpha_j(t)$ can be reasonably approximated as constants. This assumption allows us to perform the inverse analysis on a day-by-day basis, using temperature data collected daily.

In this project, we applied this assumption to evaluate the feasibility of using a Markov Chain Monte Carlo (MCMC) approach for estimating the posterior distributions of the thermal diffusivity coefficients α_j . The results demonstrate the potential of MCMC methods for capturing the underlying parameter uncertainties in pavement thermal characterization.

In the following section, we provide a brief overview of a numerical scheme used to solve the heat equation numerically and of the MCMC methodology used in this analysis.

3.3.2.2 Numerical solution of the heat equation

The Markov Chain Monte Carlo (MCMC) method requires repeated evaluation of the forward model defined by Eq. (19). To solve this equation numerically, we employed the Crank–Nicolson Method (CNM)—a finite difference technique well-suited for one-dimensional transient heat conduction problems (Crank and Nicolson, 1947). The CNM is an implicit time integration scheme that achieves second-order accuracy in both time and space, offering a favorable trade-off between numerical accuracy and stability. One of its key advantages is its unconditional stability, which makes it particularly robust for long-time simulations and inverse problems involving noisy data.

A distinctive feature of CNM is its ability to accommodate nonuniform spatial meshes, which is especially beneficial for modeling multilayer systems such as pavements. When prior knowledge indicates that the temperature gradient changes rapidly near material interfaces or boundaries, localized mesh refinement can significantly enhance solution accuracy without introducing a prohibitive computational burden. This makes CNM an ideal numerical solver for inverse heat conduction problems in heterogeneous, multilayered domains. The CNM discretization stencil is illustrated in Figure 3.21. The method is derived by averaging the Forward-Time Centered-Space (FTCS) and Backward-Time Centered-Space (BTCS) schemes. The resulting discretized form of the heat equation is expressed as:

$$\frac{T_{i+1,j}-T_{i,j}}{\Delta t}=\frac{\alpha_j}{2}\left(\frac{T_{i,j+1}-2T_{i,j}+T_{i,j-1}}{\Delta y^2}+\frac{T_{i+1,j+1}-2T_{i+1,j}+T_{i+1,j-1}}{\Delta y^2}\right) \quad (22)$$

where $T_{i+1,j}$ is the temperature at spatial node j and time step i, Δy is the spatial step size along the depth of the pavement, Δt is the time step size (see Fig. 3.21). Next, after multiplying both sides by Δt, we can rearrange the terms of the expression above to obtain

$$-\frac{r}{2}T_{i+1,j-1}+(1+r)T_{i+1,j}-\frac{r}{2}T_{i+1,j+1}=\frac{r}{2}T_{i,j-1}+(1-r)T_{i,j}+\frac{r}{2}T_{i,j+1} \quad (23)$$

where $r=\frac{\alpha\Delta t}{\Delta y^2}$ is a dimensionless parameter. The time evolution equation can be written as a tridiagonal matrix system in the form $\mathbf{A}T_{i+1}=\mathbf{B}T_i+b$, where $\mathbf{A}$ is a tridiagonal matrix with coefficients $-\frac{r}{2}$, $1+r$, and $-\frac{r}{2}$; $\mathbf{B}$ is a tridiagonal matrix with coefficients $\frac{r}{2}$, $1-r$; and $\frac{r}{2}$. T^{n+1} and T^n are temperature vectors at times t_{i+1} and t_i, respectively. Finally, b is a vector that includes contributions from the boundary conditions (See Crank and Nicolson (1947) for a detailed description of this method).

In the pavement sections analyzed in this study, we use a discretization in both time and space to solve the heat equation numerically. At the interfaces between layers, we enforce continuity of the temperature field and heat flux, ensuring physically consistent transitions across material boundaries accomplished by matching the temperature and flux from both sides of the interface.

Regarding the boundary conditions, we prescribe the measured temperatures at the topmost and bottommost sensors as Dirichlet conditions. The initial temperature profile is defined using the measurements from all sensors in the thermocouple array at the initial time $t=t_0$. The forward model then simulates the temperature field over a 24-hour period, enabling comparison between observed and predicted values, which is useful for inverse modeling and uncertainty quantification.

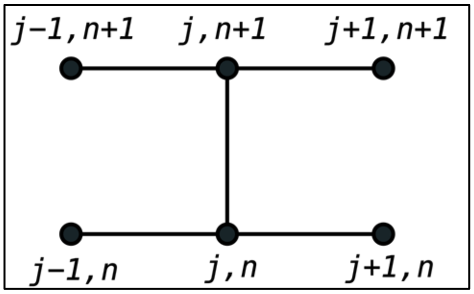

Figure 3.21 Crank-Nicolson Method discretization scheme.

3.3.2.3 Mathematical formulation of MCMC for inverse problems

We have mentioned earlier that the MCMC is used to perform the identification of the thermal diffusivities of the pavement layers. The MCMC relies on the Bayes' theorem, which constitutes the core of Bayesian inference, and it is defined through the following expression:

$$P(\alpha|T) = \frac{p(Y|\alpha)p(\alpha)}{P(T)} \tag{24}$$

In this expression, we are interested in determining the probability distribution $p(\alpha|T)$, also known as posterior, of the parameters α of a given model $\mathcal{M}(\cdot)$ (i.e., heat equation), such that $T = \mathcal{M}(\alpha) + \varepsilon$, where T are the model outputs (temperature) and ε is the noise representing an aleatoric uncertainty. Therefore, we want to find a probabilistic model for the parameters that maximize the likelihood $p(T|\alpha)$ that the data Y was generated by the model with parameters α. To this end, we have to assume a prior knowledge of the probability distribution $p(\alpha)$ of the parameters in order to create an updating scheme based on the Bayes' theorem in order to obtain the posterior distribution, where $p(T)$ denotes the probability distribution of the data.

To this end, MCMC generates a sequence of samples that approximates the posterior distribution by constructing a Markov chain with the posterior as its stationary distribution. One of the most widely used sampling algorithms is the Metropolis-Hastings algorithm, which proceeds as follows:

1. Initialize with a starting parameter α_0;
2. At iteration k, propose a new parameter α^* from a proposal distribution $q(\alpha^*|\alpha_i)$;
3. Compute the acceptance ratio as:

$$A(\alpha^*|\alpha_k) = \min\left[1, \frac{P(Y|\theta^*)p(\theta^*)q(\theta^*|\theta_i)}{P(Y|\theta_i)p(\theta_i)q(\theta_i|\theta^*)}\right] \tag{25}$$

4. Accept α^* as $\alpha_{k+1}$with probability $A(\alpha^*, \alpha_i)$; otherwise, set $\alpha_{i+1} = \alpha_i$.

The chain converges to the posterior distribution after sufficient iterations, enabling parameter estimation (e.g., posterior mean value) and uncertainty quantification (e.g., credible intervals). In the context of inverse problems, the likelihood function $p(T|\alpha)$ is defined based on the forward model that relates the physical real-world behavior and the observed data to the unknown parameters.

Chapter 4: Spectral Analysis for Temperature Data

In this task, the research team applied two spectral analysis techniques to investigate the temperature data collected over the past 20 years from thermocouple trees installed in selected pavement sections. The analysis focused on both flexible pavements (cells 2, 3, and 4) and rigid pavements (cells 12 and 13), as detailed in Chapter 3. However, the analysis in this report will focus only on cell 2, 12, and 13, because the observations based on these cells are easily extended to the other sections. Thus, although a detailed analysis on the other cells is not presented here, the processed signals and filter data are available for future investigations.

The objective of this task is to examine the relationship between the thermal performance of pavements and the spectral properties of temperature fluctuations, with the goal of identifying potential indicators for assessing the life-cycle performance of pavement structures. To ensure the robustness of the conclusions drawn, both Fourier and wavelet analyses were employed. By leveraging the strengths of each method, we aim to achieve consistent and reliable results. We expect both techniques to yield similar patterns and trends in the spectral properties of the temperature field.

Using the filter modeling approach described in Section 3.3.1.1, we treated the temperature fluctuation recorded by adjacent thermocouples as input and output signals of a dynamic system. Specifically, the signal measured at the top of a pavement segment is considered the input, and the signal at the bottom is the output—resulting in a linear filter model representing heat conduction behavior. By computing the FRF either in the frequency domain (via Fourier analysis) or in the joint time-frequency domain (via wavelet analysis), we extracted the amplitude, phase shift, and coherence functions of the temperature signals. These quantities were further analyzed to study their temporal evolution, with Fourier analysis offering a coarser time resolution and wavelet analysis providing finer, more localized time-frequency insights.

For each pavement section, FRFs were calculated for every pair of adjacent thermocouples within the corresponding thermocouple tree.

Table 4.1 summarizes the number of thermocouples available per cell over two distinct time periods used for spectral analysis. It is important to note that temperature signals containing extensive data gaps were excluded from the analysis presented in this report. Furthermore, Table 4.2 lists the sensors that were not used due to significant data corruption, for example, due to the presence of large missing segments of the signal. An example of a signal with missing gaps that are too large to be reliably recovered is presented in Figure 4.1. This signal corresponds to the measurement of sensor 113 in cell 2.

Table 4.1 Number of thermocouples per cell.

Cell	**Number of thermocouples**	
	1998-2008	***2008-2022 (2015 for cell 2)***
2	1	1
3	1	1
4	7	1
12	4	4
13	1	1

Table 4.2 Sensors not used in the present analysis due to the presence of large missing segments.

Cell	**Dismissed sensor data**	
	1998-2008	***2008-2022 (2015 for cell 2)***
2	None	113
3	1, 2, 11	None
4	1, 2, 11, 21, 22, 40-53	None
12	38, 41, 42	38, 41, 42
13	None	None

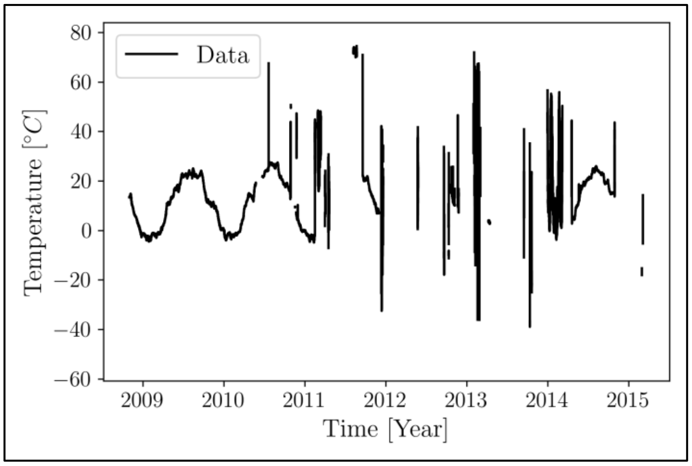

Figure 4.1 Signal containing large missing segments.

The first step of this analysis consisted in the identification of the signal that can be reconstructed using compressed sensing and with the removal of artifacts. After the identification of the "healthy" signals, we proceed with the reconstruction of the signals with missing data. Additionally, we include the precipitation data for the corresponding time periods as a reference to aid the determination of potential influences on the time-varying behavior of the phase shift. Next, the recovered signals are used in the spectral analysis developed by the research team. In this report, we present the spectral analyses corresponding to cells 2, 12, and 13.

In the ensuing analysis, we consider that a negative phase shift between the input and the output signals means that the output is delayed in comparison to the input signal. In Figure 4.2, where the horizontal axis represents the time domain, we can assume that the red oscillating function is the input signal and that the blue oscillating function is the output, which has a delay equal to θ.

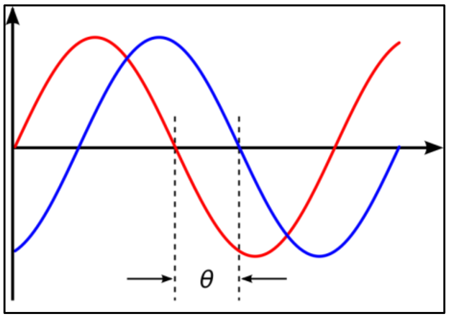

Figure 4.2 Delay between the input (red) and the output (blue) signal representing a negative phase shift.

4.1 Flexible pavement

The data from cells 2, 3, and 4 are divided into two groups. Group A corresponds to data acquired between 1998 and 2008, while Group B includes data collected between 2008 and 2022. The only exception is cell 2, where Group B includes data only from 2008 to 2015. Fourier and wavelet analyses were performed to characterize the time-varying behavior of the FRF properties derived from filter models of pavement segments. The results for magnitude, phase shift, and coherence are presented for the selected cells and thermocouple trees, beginning with cell 2 (Groups A and B). Furthermore, the figures included in this section show a comparison of the coherence, magnitude (gain), and phase shift of the filters estimated using the temperature time histories. Figures (a) present the results obtained from the Fourier analysis described in Section 3.3.1.2, while figures (b) show the results from the wavelet analysis introduced in Section 3.3.1.3. The objective of this comparison is twofold. On the one hand, we aim to validate the results by demonstrating that similar outcomes can be achieved using two distinct methods. On the other hand, we seek to determine which technique offers better resolution in the time domain.

Figure 4.3 and Figure 4.4 show the coherence functions obtained using both methods for all modeled filters in cell 2, Group A and Group B, respectively. We observe that both Fourier and wavelet techniques yield comparable coherence results. However, the wavelet analysis offers superior temporal resolution, making it more effective in identifying time-localized behaviors. Additionally, we note that the coherence function is strongly material-dependent. For instance, in Figure 4.3 (cell 2, Group A), filters 1 and 2, which model the asphalt layer, exhibit high and relatively uniform coherence. This behavior reflects the fact that asphalt is less sensitive to heat conduction compared to the granular base and subgrade layers. In contrast, the base and clay layers display greater sensitivity to precipitation, resulting in periodic losses of linearity in the filter model. This phenomenon manifests as oscillations in the coherence function, and similar behavior is observed in the FRF magnitude and phase shift.

This analysis was repeated for the data in Group B (see Figure 4.4a and Figure 4.4b), and the results were consistent with those of Group A. These findings confirm the sensitivity and reliability of the filter modeling approach in capturing the characteristics of heat conduction across different pavement layers. The coherence function proves to be an effective indicator of the thermal behavior of multilayer pavement structures. Next, we present the magnitude and phase shift of the FRF, demonstrating that these quantities carry rich information about the thermal properties of the individual pavement layers.

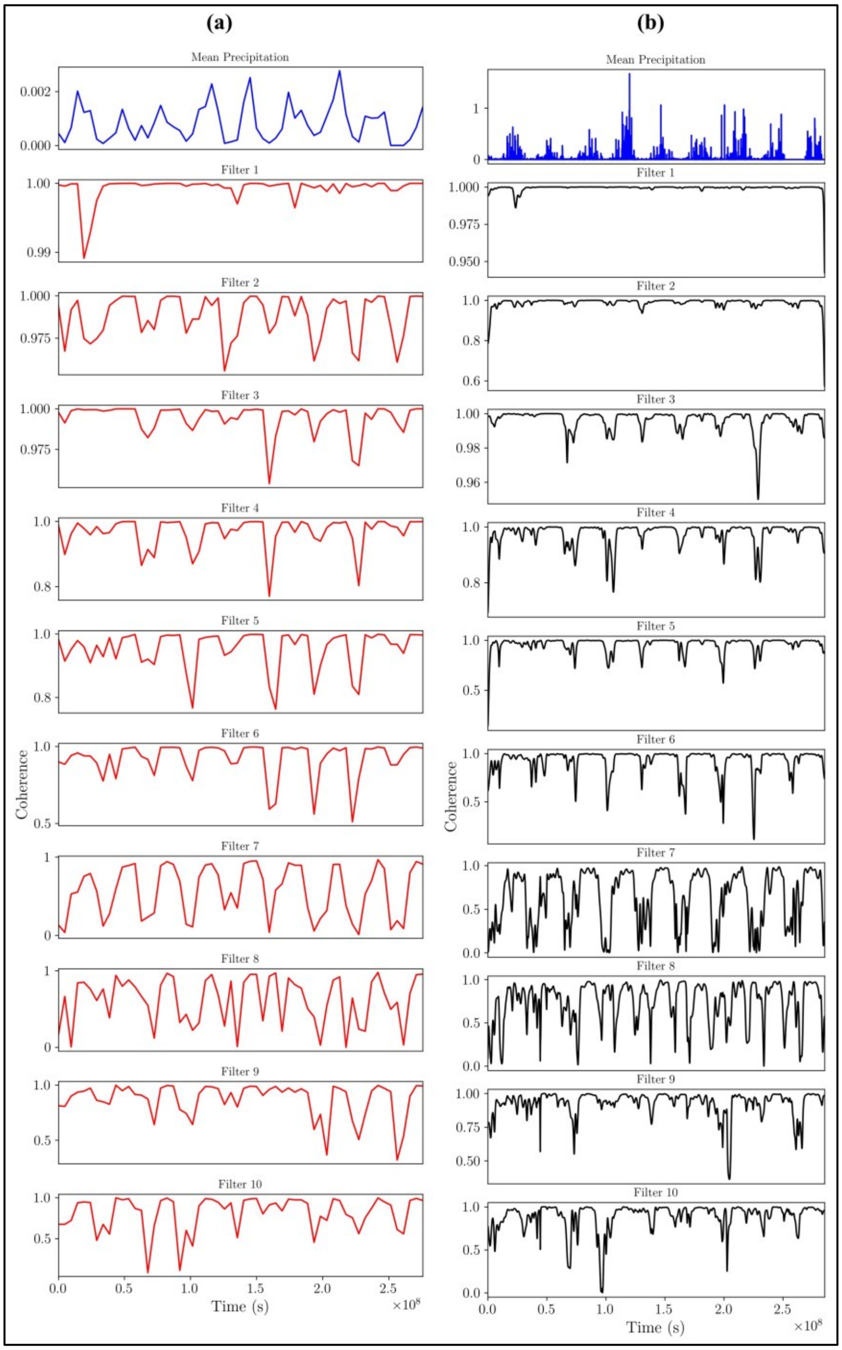

Figure 4.3 Coherence for cell 2 (1998-2008): a) Fourier and b) wavelet analyses.

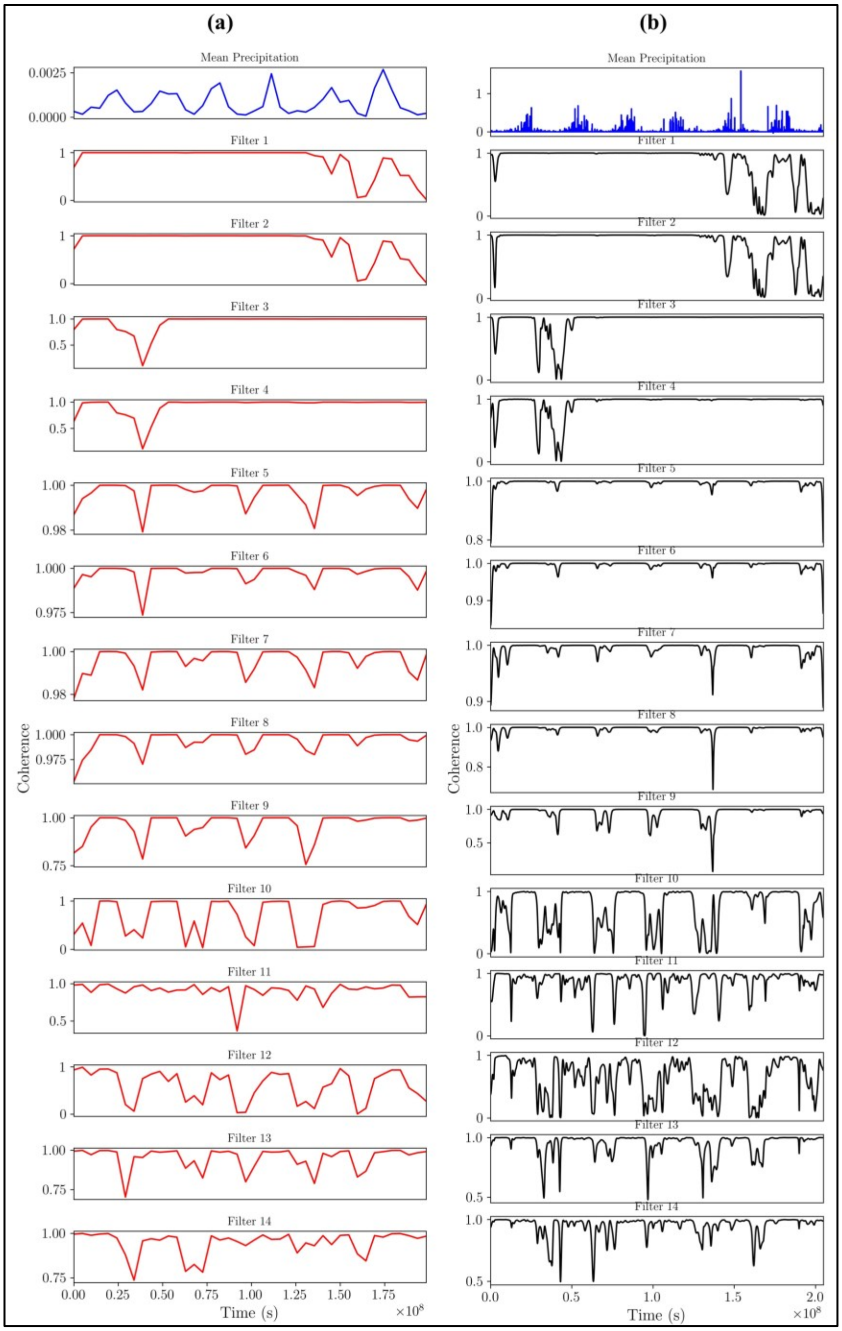

Figure 4.4 Coherence for cell 2 (2008-2015): a) Fourier and b) wavelet analyses.

Next, we compare the behavior of the magnitude of the FRF and the phase shift across different pavement layers. First, it is evident that both the magnitude and phase shift exhibit time-dependent behavior, which may be attributed to the aging and densification of materials, along with changes in their thermal properties. Additionally, each layer demonstrates a distinct temporal pattern and responds differently to variations in average temperature and precipitation regimes.

While these observations are promising, further investigation is necessary to clarify potential correlations between filter properties and environmental conditions. Based on the results presented in **Figure 4.5**, filters 2 and 3—located within the asphalt layer—exhibit a slight decrease in FRF magnitude over time. This trend could be associated with the evolving mechanical and thermal properties of asphalt. A reduction in the phase shift magnitude suggests a potential decrease in heat conduction through the asphalt. However, additional analysis is needed to validate this hypothesis.

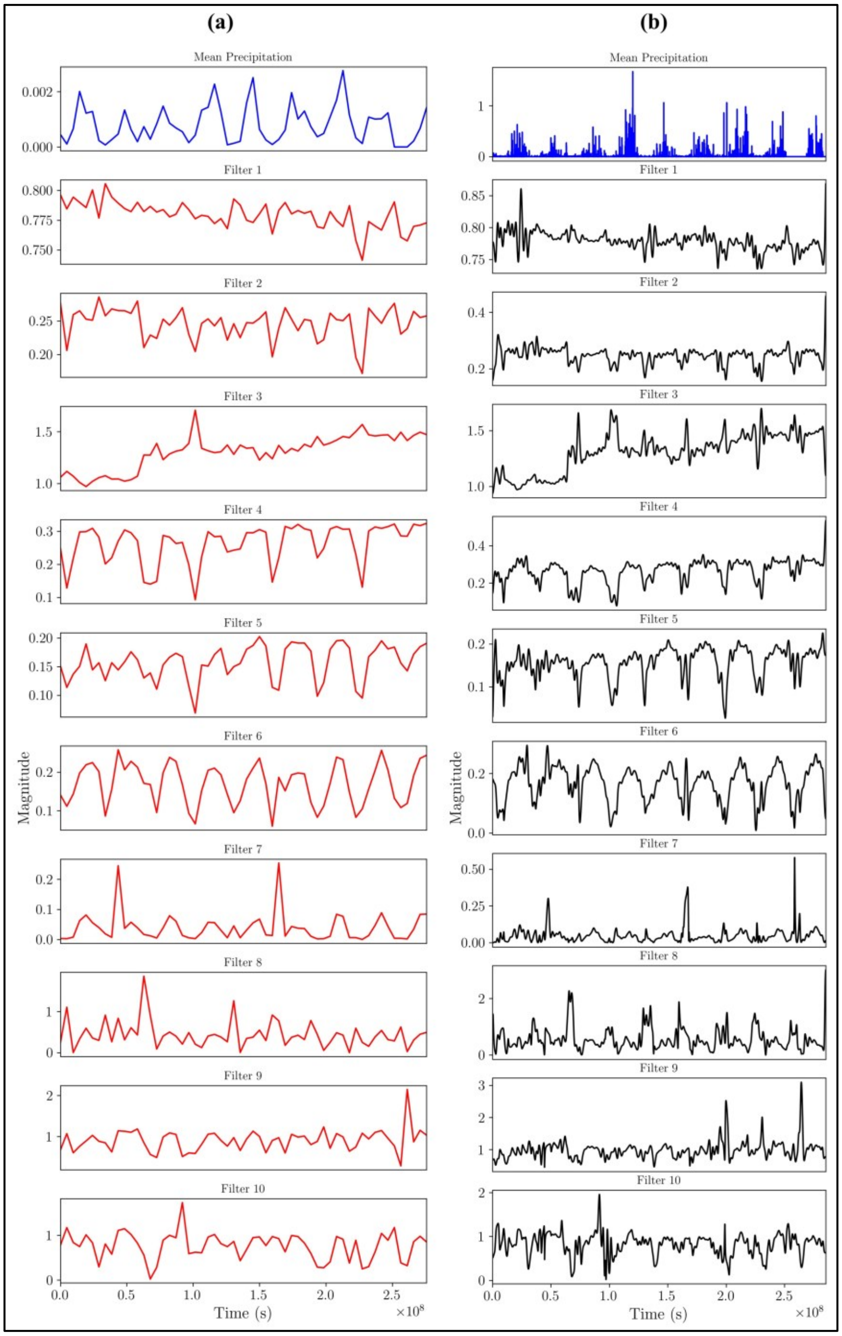

Figure 4.5 FRF magnitude for cell 2 (1998-2008) : a) Fourier and b) wavelet analyses.

Notably, filter 3, which corresponds to the interface between the asphalt and the base, shows a significant increase in FRF magnitude over time. This trend indicates an increase in thermal conductivity at the interface. Moreover, the base layer appears to show an inverse correlation with precipitation—becoming more thermally conductive during wetter periods—whereas the subgrade appears less sensitive to weather conditions.

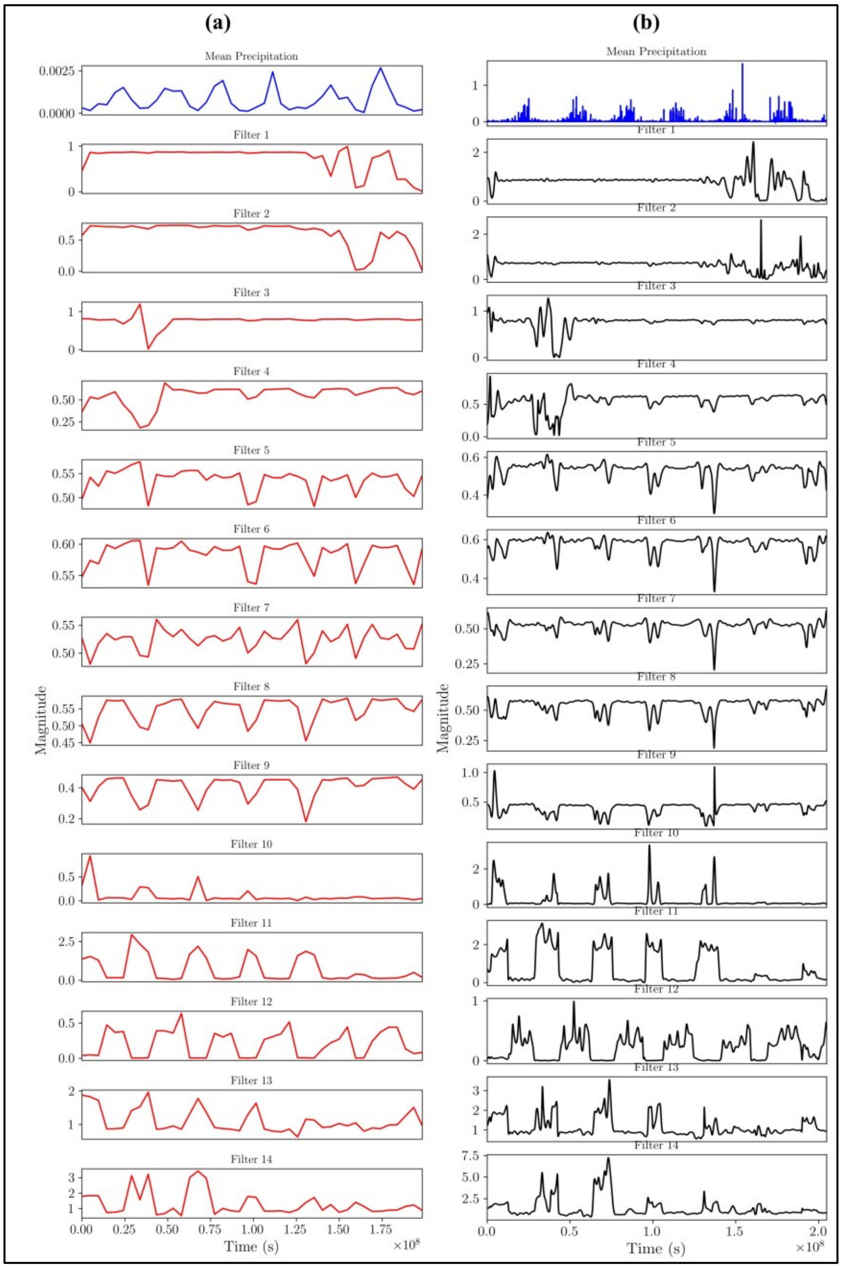

Figure 4.6 FRF magnitude for cell 2 (2008-2015): a) Fourier and b) wavelet analyses.

After the pavement was reconstructed, the spectral properties of heat transport changed markedly. Despite this shift, the individual behaviors of each layer remain distinguishable, particularly when analyzing the FRF magnitude profiles.

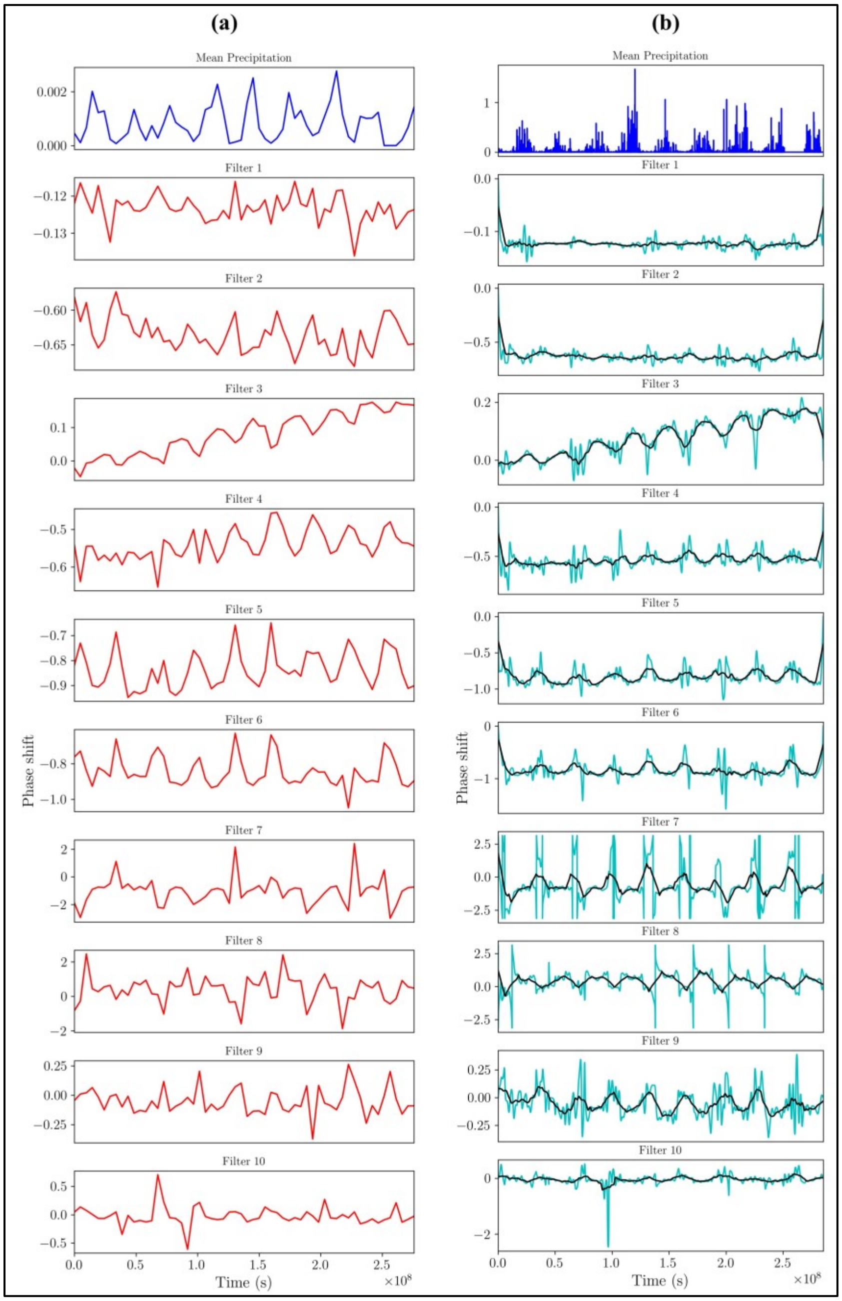

Figure 4.7 FRF phase shift for cell 2 (1998-2008): a) Fourier and b) wavelet analyses.

The evolution of the phase shift, as illustrated in Figure 4.7 (Group A) and Figure 4.8 (Group B), also reveals significant insights. For example, during the 1998–2008 period, the interface between the asphalt and base layers plays a prominent role in the conduction process, as evidenced by a positive phase shift. Additional investigation is warranted to understand the physical mechanisms driving this phenomenon. After reconstruction, the overall phase shift profile changes considerably; however, the distinct thermal characteristics of each layer remain apparent (see Figure 4.8). Notably, the base layer becomes less sensitive to environmental variability over time, as indicated by the diminished amplitude of phase shift oscillations in filters 7 through 10. This trend could reflect changes in base compaction or moisture retention and should be explored further.

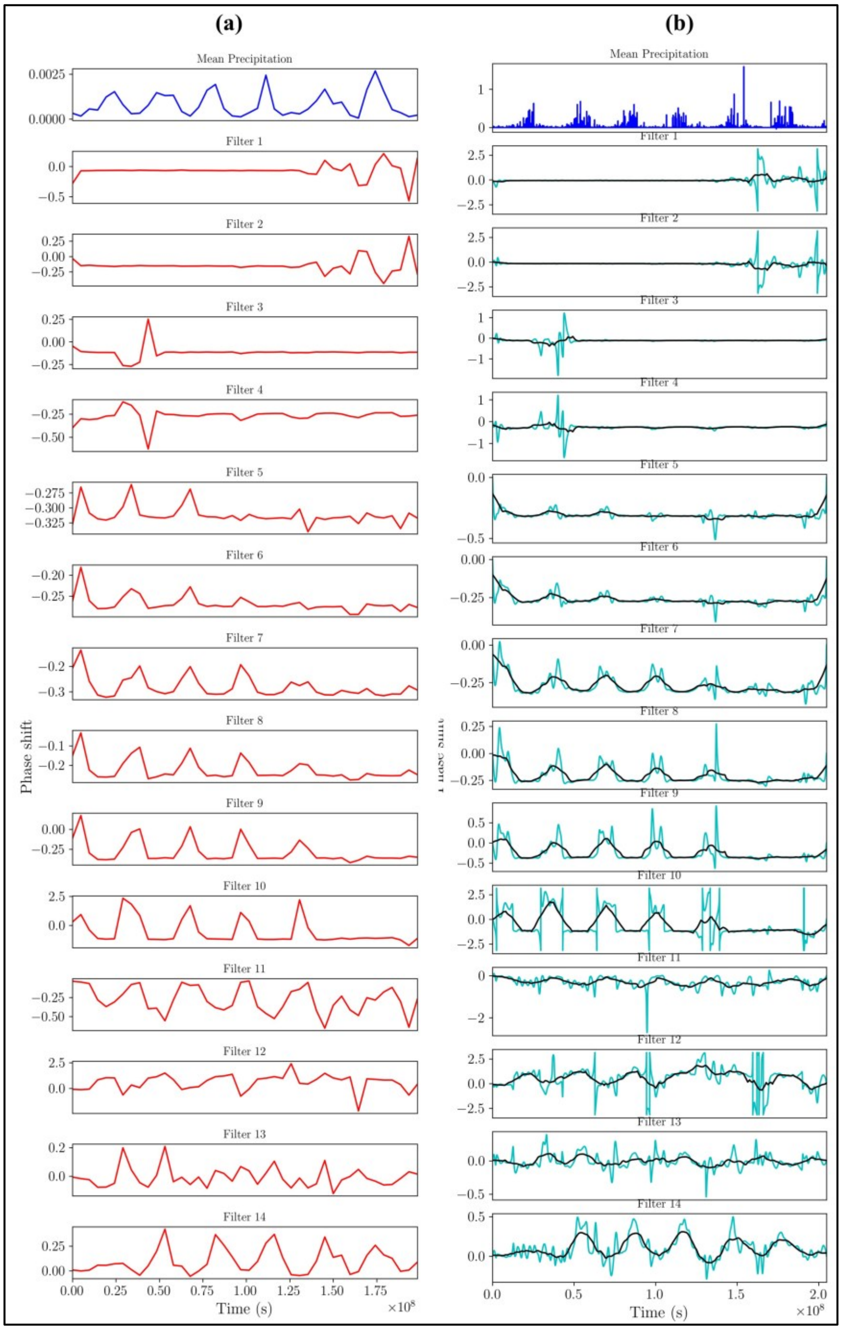

Figure 4.8 FRF phase shift for cell 2 (2008-2015): a) Fourier and b) wavelet analyses.

To complement these observations, Figure 4.9 (Group A) and Figure 4.10 (Group B) present three sets of quantities derived using both Fourier and wavelet analyses. In each figure: The left panel displays the slope of the phase shift over time for sensors placed at various pavement depths. The right panel presents the mean phase shift over time across the same sensor set. The center panel shows the mean FRF magnitude over time for all sensors in the thermocouple tree.

These plots collectively define a filter profile of the pavement, which may serve as a diagnostic signature for detecting structural anomalies or degradation over time. Comparing the two figures, we observe that after reconstruction, the upper layers of the pavement exhibit a flattened filter profile, suggesting increased thermal conductivity near the surface. This outcome highlights the potential of spectral filtering methods to track changes in thermal performance due to structural modifications or environmental influences.

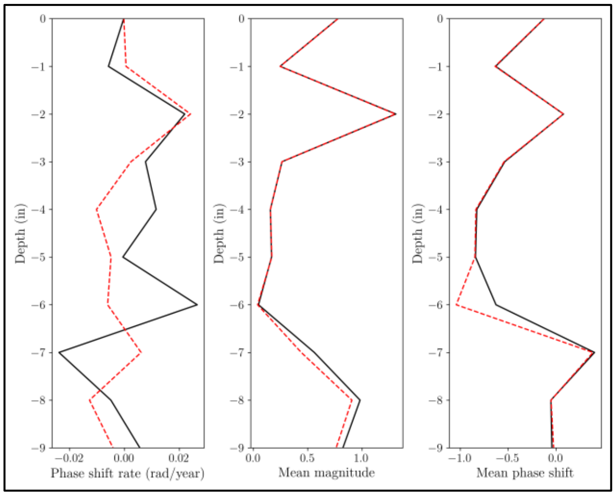

Figure 4.9 Slope of the phase shift (left), mean FRF amplitude (middle), mean phase shift (right) for cell 2 (1998-2008): Fourier (red dashed line) and wavelet analyses (black solid line).

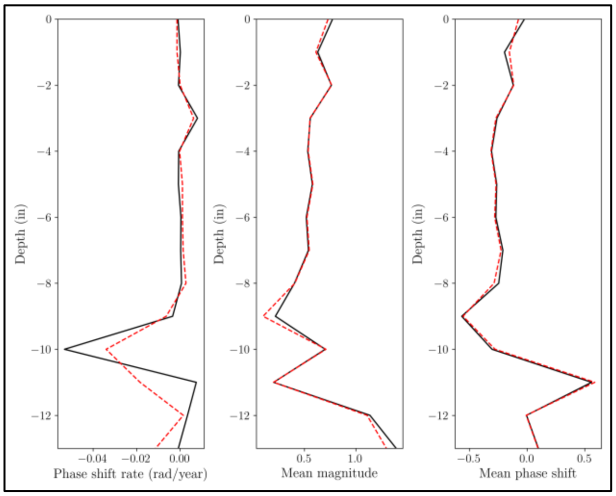

Figure 4.10 Slope of the phase shift (left), mean FRF amplitude (middle), mean phase shift (right) for cell 2 (2008-2015): Fourier (red dashed line) and wavelet analyses (black solid line).

4.2 Rigid Pavement

The analysis presented in the previous section provides key insights into the dynamics of thermal conduction in flexible pavements. In this section, we focus on cells 12 and 13. Although the analysis was conducted using data from all thermocouples in cell 12, only the data from the first thermocouple is used here to introduce the developed methodology. Moreover, since the results obtained with Fourier analysis are similar to those from wavelet analysis, we present only the wavelet-based graphics in this section due to their superior time-domain localization.

Figure 4.11 shows the coherence, FRF magnitude, and phase shift for all filters modeling the heat conduction dynamics in the section of cell 12 containing the first thermocouple. The coherence indicates that the linear filter model is suitable for representing heat conduction within the concrete layer. However, we observe that the properties of the filter modeling the lower part of the concrete layer change significantly over time, unlike those modeling the upper part. This difference could be explained by the proximity of the lower part to the base and thus to humidity, as suggested by the correlation with precipitation through seasonal fluctuations in the filter properties. Additionally, the magnitude and phase shift at the interface exhibit a notable time-dependent behavior, both increasing over time, possibly reflecting enhanced heat conduction at the interface between the concrete layer and the base.

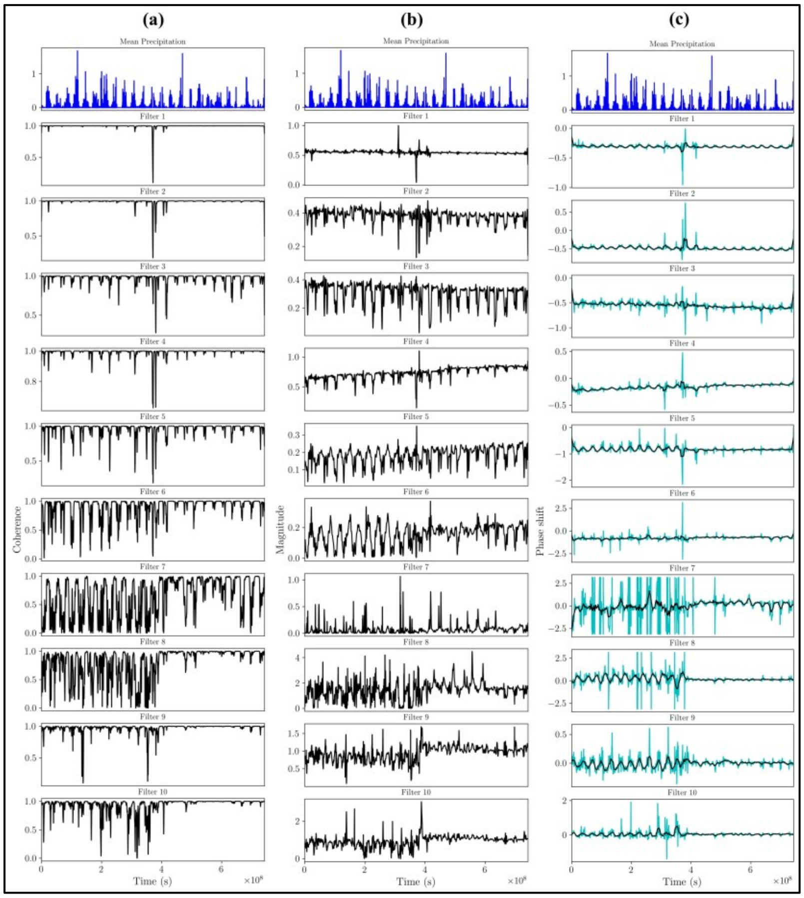

Figure 4.11 Wavelet a) coherence, b) FRF magnitude, and c) phase shift for cell 12.

A significant long perturbation at the subgrade was discovered. However, further investigation is necessary to explain this perturbation in the coherence, FRF magnitude, and phase shift. Figure 4.12 shows the coherence, FRF magnitude, and phase shift for cell 13. Figure 4.13 presents the heat conduction profile for cell 12, which resembles that of cell 13. Here, we observe a clear correlation with weather conditions but no significant trend in magnitude or phase shift. Nonetheless, a notable perturbation is again observed at the subgrade and base, the cause of which remains undetermined but could be related to factors such as fluctuations of the relatively shallow groundwater table.

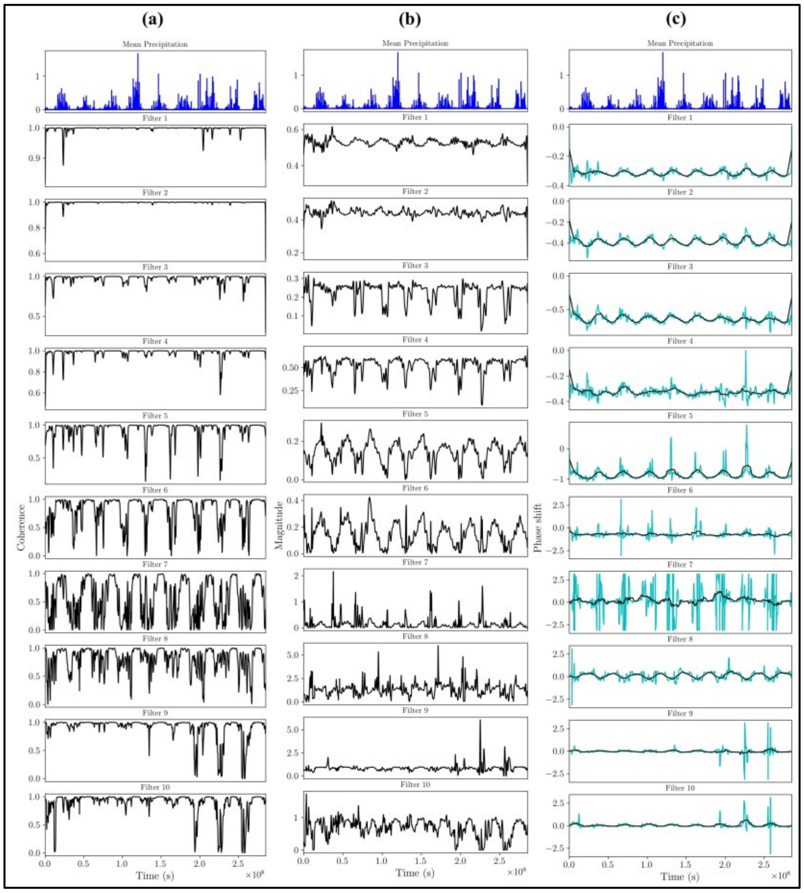

Figure 4.12 Wavelet a) coherence, b) FRF magnitude, and c) phase shift for cell 13.

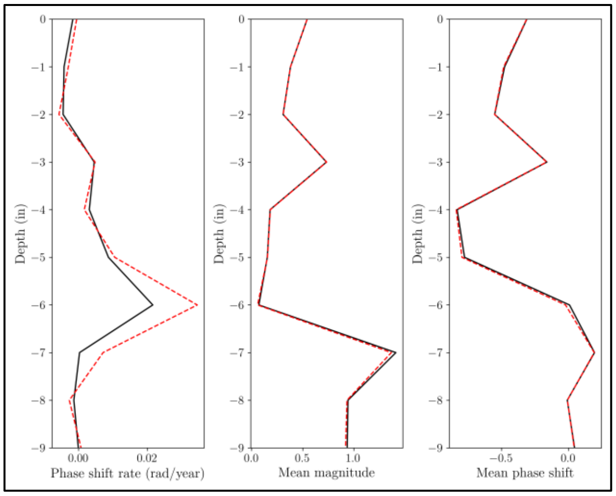

Figure 4.13 Slope of the phase shift (left), mean FRF amplitude (middle), mean phase shift (right) for cell 12: Fourier (red dashed line) and wavelet analyses (black solid line).

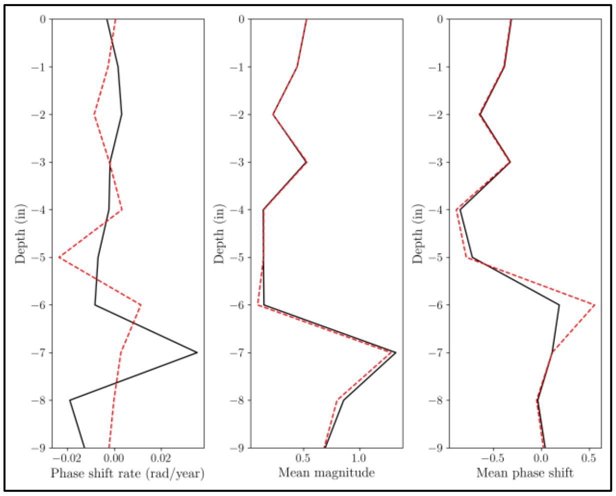

Figure 4.14 Slope of the phase shift (left), mean FRF amplitude (middle), mean phase shift (right) for cell 13: Fourier (red dashed line) and wavelet analyses (black solid line).

4.3 Discussion

The results presented above demonstrate that the thermodynamic behavior of both flexible and rigid pavements is effectively captured by the properties of the modeled filters. These findings indicate that the filters' time-dependent characteristics are closely linked to the evolving environmental conditions affecting the pavement, including ageing and weather variations. Additionally, we observe that both the phase shift and magnitude of the filters vary with depth and depend on the spacing between sensors. Notably, the interfaces between layers exhibit particularly intriguing behaviors, showing significant time-dependent influences on both phase shift and magnitude. While further investigation is needed to pinpoint the exact causes of these phenomena, we are confident that they correlate with pavement performance, potentially reflecting processes such as densification and compaction of granular materials, as well as variations in their thermal properties.

Chapter 5: Probabilistic Analysis and Pavement Degradation Prediction

In this research project, we demonstrate—through theoretical analysis and real-world data—that proper treatment of temperature measurements can yield sensitive indicators of pavement condition for both flexible and rigid systems. To accomplish this objective, we developed a probabilistic framework that enables rigorous uncertainty quantification of the thermal diffusivity coefficients associated with different pavement layers over a 24-hour period. To this end, we consider the data from Cell 12. Specifically, the research team employed an MCMC approach to predict the temperature field at each sensor within the thermocouple tree and estimate the probability density functions of the thermal parameters corresponding to each material layer. We considered 3 different days as examples in our analysis: 04/15/1998, 06/15/2009, and 02/10/2021.

The posterior distributions of the thermal diffusivity parameters α_1, α_2, and α_3—corresponding to concrete, aggregate base, and clay, respectively—were estimated using 12 independent Markov chains, each generating 3,000 samples, resulting in a total of 36,000 samples per parameter. We adopted uniform, non-informative prior distributions for all parameters and used a log-likelihood function based on the discrepancy between observed and simulated temperatures. The simulated field was computed by solving the forward heat equation using samples drawn from the posterior distributions of each thermal diffusivity parameter α_i. The residuals are defined as the difference between observed and predicted temperatures.

We employed the proposed uncertainty quantification methodology to analyze the first day of measured temperatures. Figure 5.1 shows the measured, predicted average, and residual temperature fields. The results show a good agreement between the real-world data and the results obtained using the MCMC method. In addition, the residuals are minimal, with a maximum absolute error of approximately 0.46 °C, indicating that the methodology accurately captures the system's thermal behavior.

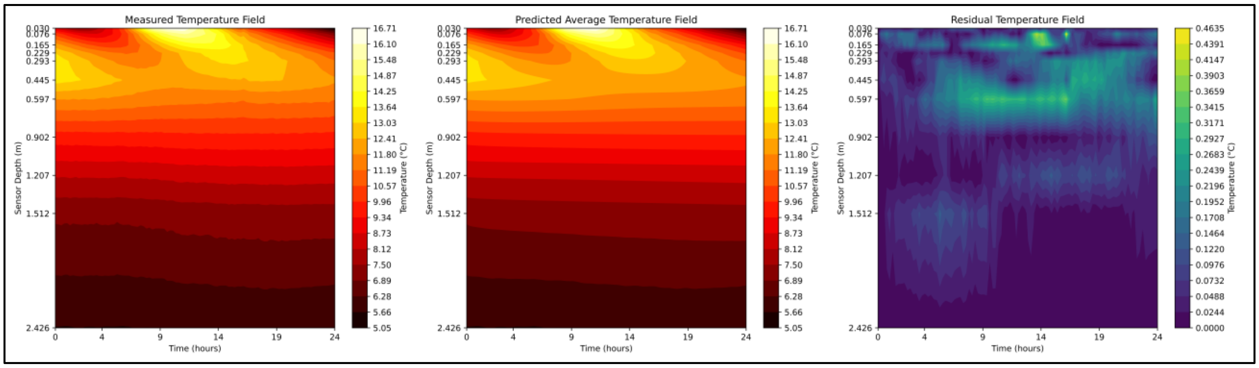

Figure 5.1 The measured, predicted average, and residual temperature fields for 04/15/1998.

Furthermore, Figure 5.2 illustrates the observed temperature field, the predicted average temperature field, and the resulting residual temperature field for the second analyzed day. The results show strong agreement between the predicted and measured temperature profiles, indicating that the inference framework captures the system's thermal behavior with high fidelity. The residuals are generally small, with a maximum absolute residual of approximately 0.85°C, confirming the accuracy of the proposed computational model.

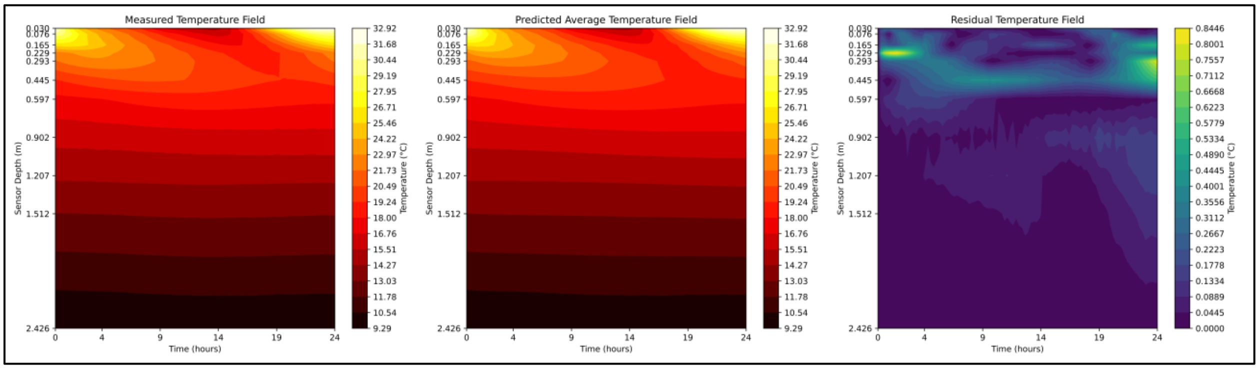

Figure 5.2 The measured, predicted average, and residual temperature fields for 06/15/2009.

Next, we applied the proposed methodology for the temperature field on the third day. The measured, predicted average, and residual temperature fields are plotted in Figure 5.3. The results indicate a strong agreement between the predicted and observed profiles, even with higher temperatures in the bottom layer and lower temperatures near the surface of the pavement. Compared to the second day, the residuals are slightly larger, exceeding 1 °C, but the maximum absolute residual error remains low, at approximately 1.17 °C.

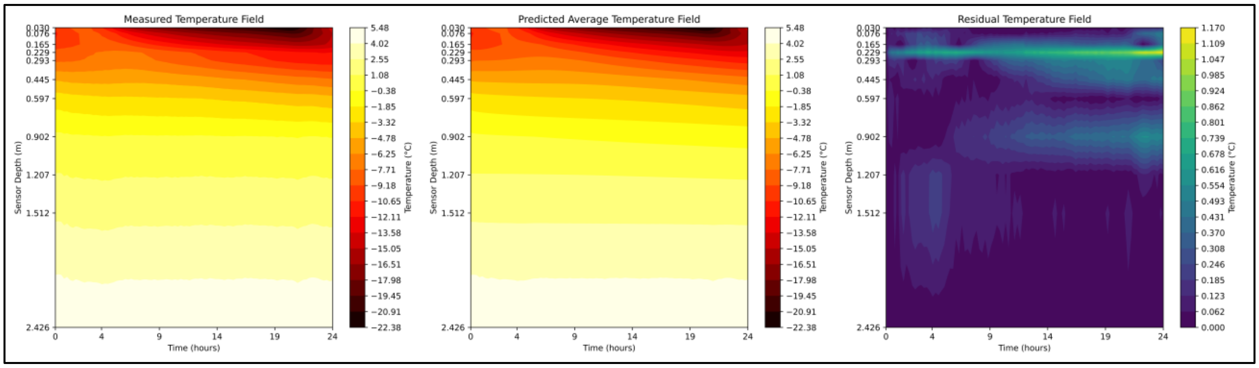

Figure 5.3 The measured, predicted average, and residual temperature fields for 02/10/2021.

Next, we applied Kernel Density Estimation (KDE) to estimate the posterior probability density functions of the thermal diffusivity parameters across the analyzed days. As illustrated in Figure 5.4, the posterior distributions for concrete and clay appear approximately Gaussian, centered around their respective mean values. In contrast, the distribution for the aggregate base layer exhibits a more irregular shape for the third day, indicating that a better calibration strategy must be employed. This behavior is expected, as concrete and clay tend to have more consistent and well-characterized thermal properties, while the aggregate base layer is typically more heterogeneous and less predictable.

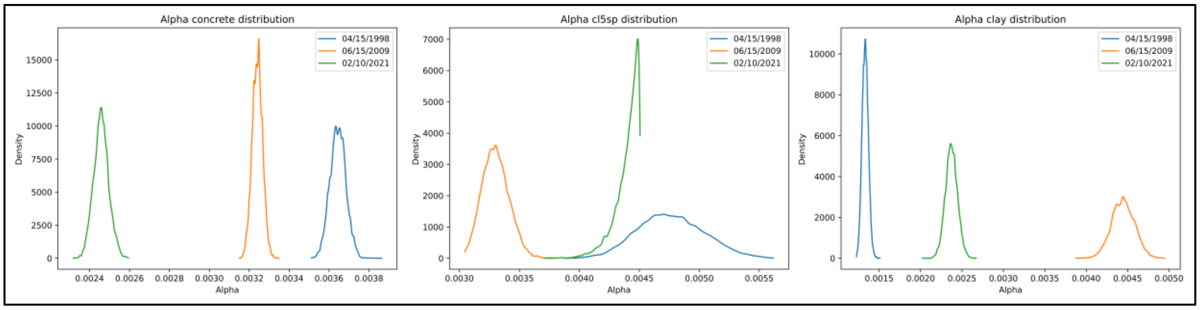

Figure 5.4 Posterior probability distributions of the thermal diffusivity parameters for the concrete, CL5sp (aggregate base), and clay layers for all three days analyzed. The distributions were estimated using KDE.

Finally, analysis of all posterior distribution plots reveals a decrease in the thermal diffusivity of the concrete layer. The aggregate base layer exhibits temporal variability in its thermal diffusivity, as expected. While this behavior is expected due to the heterogeneous nature of the material, it is difficult to conclusively attribute these changes to physical deterioration. External environmental factors, such as moisture content and precipitation, likely play a significant role in its thermal response. Moreover, we observe an increase in the thermal diffusivity coefficient a_3 for the clay layer, potentially suggesting changes in the physical properties of this material, such as the thermal conductivity or soil humidity.

Chapter 6: Summary, Conclusions and Recommendations

6.1 Summary

This research study developed a computational tool to predict pavement performance using long-term temperature data collected from thermocouple trees embedded in pavement sections at the MnROAD research facility. The study focused on three flexible (cells 2, 3, and 4) and two rigid (cells 12 and 13) pavement sections, leveraging temperature measurements to analyze thermal behavior and its impact on pavement condition. The research comprised three main components:

1) **Data Collection and Preprocessing**. Temperature data were gathered from thermocouple trees, supplemented by weather data (air temperature, humidity, and precipitation) from MnROAD's weather stations. Challenges such as missing data, noise, and artifacts were addressed using compressed sampling (CS) to reconstruct incomplete signals, ensuring a uniform 15-minute sampling interval.
2) **Spectral Analysis**. Two techniques, Fourier Transform and Wavelet Analysis, were applied to model pavement layers as a cascade of filters, characterizing the time-varying thermal properties (gain and phase shift) of pavement sections. These methods provided insights into heat conduction dynamics, with wavelet analysis offering superior temporal resolution for capturing non-stationary behaviors.
3) **Probabilistic Analysis**. A Markov Chain Monte Carlo (MCMC) approach, based on Bayesian inference, was used to estimate thermal diffusivity coefficients for pavement layers. The method employed the Crank-Nicolson numerical scheme to solve the one-dimensional heat equation, enabling uncertainty quantification and validation of spectral analysis results.

All computational methods were implemented in a modular, object-oriented Python package, publicly available on GitHub with reproducible Jupyter notebook examples. The study demonstrated that thermocouple-derived temperature data, when processed with advanced spectral and probabilistic tools, can reliably detect changes in pavement material properties due to aging, moisture, or compaction, supporting long-term infrastructure management.

6.2 Conclusions

Based on the research conducted, the following conclusions can be drawn:

- Thermocouple trees provide a robust method for monitoring pavement thermal behavior, capturing daily and yearly temperature fluctuations that reflect material and environmental interactions. The filter modeling approach, using spectral properties (gain, phase shift, and coherence), effectively identifies time-dependent changes in pavement thermal performance.
- Compressed sampling effectively reconstructed missing data in temperature signals, enabling reliable spectral and probabilistic analyses. The data quality assessment and artifact removal

processes ensured that only healthy signal segments were used, enhancing the accuracy of the results.

- Both Fourier and Wavelet analyses successfully characterized the thermal properties of pavement layers. Wavelet analysis, particularly with Generalized Harmonic Wavelets, proved superior for its finer temporal resolution, enabling the detection of transient thermal phenomena linked to environmental events like precipitation.
- The MCMC-based probabilistic framework accurately estimated thermal diffusivity coefficients, with residuals between observed and predicted temperatures typically below 1.17°C. The approach provided robust uncertainty quantification, confirming the reliability of thermal parameters as indicators of pavement condition.
- The study revealed distinct thermal responses across pavement layers. Asphalt layers showed high coherence and uniform thermal behavior, while base and subgrade layers were more sensitive to environmental factors like precipitation. Interfaces between layers exhibited significant time-dependent changes, potentially linked to densification or moisture effects.

6.3 Recommendations

The findings of this study represent a very good start in developing a computational tool for reliable prediction of pavement performance based on temperature data. However, this research effort needs to be continued to address the following key issues:

- While this study focused on thermal properties, future research should integrate fracture mechanics models (e.g., cohesive zone models) to correlate thermal behavior with mechanical performance, such as crack initiation and propagation, to provide a more comprehensive assessment of pavement durability.
- Further investigation is needed to quantify the relationship between environmental factors (e.g., precipitation, humidity) and changes in thermal properties, particularly at layer interfaces. This could enhance predictive models for pavement degradation under varying weather conditions.
- Develop real-time data processing pipelines using the proposed Python package to enable continuous pavement condition monitoring. This could involve integrating sensor data with machine learning models to predict performance trends dynamically.
- Extend the analysis to additional MnROAD cells and other pavement types to validate the generalizability of the spectral and probabilistic methods. This would strengthen the tool’s applicability across different regions and pavement designs.
- Refine data quality assessment thresholds (e.g., MSE, R^2, Frobenius norm) to optimize the identification of reconstructed signal segments. Explore advanced machine learning techniques for automated detection of data corruption.
- Partner with MnDOT and other transportation agencies to deploy the computational tool in operational settings, integrating it with existing pavement management systems to support data-driven decision-making.

References

Al-Omari, A., Khasawneh, M., & Barakat, M. (2022). Forecasting flexible pavement temperatures by Fourier series formulae using MATLAB. *Jordan Journal of Civil Engineering, 16.*

Alavi, M., Pouranian, M., & Hajj, E. (2014). Prediction of asphalt pavement temperature profile with finite control volume method. *Transportation Research Record, 2456*, 96–106. https://doi.org/10.3141/2456-10

Al-Qadi, L., Loulizi, A., Elseifi, M., & Lahouar, S. (2004). The Virginia Smart Road: The impact of pavement instrumentation on understanding pavement performance. In *Proceedings of the Technology Sessions, AAPT 2004* (pp. 427–465). Baton Rouge, LA, USA.

Allen, J. B., & Rabiner, L. R. (1977). A unified approach to short-time Fourier analysis and synthesis. *Proceedings of the IEEE, 65*(11), 1558–1564. https://doi.org/10.1109/PROC.1977.10770

Bajwa, R., Coleri, E., Rajagopal, R., Varaiya, P., & Flores, C. (2020). Pavement performance assessment using a cost-effective wireless accelerometer system. *Computer-Aided Civil and Infrastructure Engineering, 35*, 1009–1022. https://doi.org/10.1111/mice.12544

Bajwa, R., Rajagopal, R., Coleri, E., Varaiya, P., & Flores, C. (2013). In-pavement wireless weigh-in-motion. In *Proceedings of the 12th International Conference on Information Processing in Sensor Networks* (pp. …). ACM. https://doi.org/10.1145/2461381.2461397

Bajwa, R., Rajagopal, R., Variajya, P., & Kavaler, R. (2011). In-pavement wireless sensor network for vehicle classification. In *Proceedings of the 10th ACM/IEEE International Conference on Information Processing in Sensor Networks* (Chicago, IL, USA).

Barnes, R. (2010). MnROAD data mining, evaluation and quantification, Phase I (Report). Minnesota Department of Transportation. https://mdl.mndot.gov/_flysystem/fedora/2023-01/201026.pdf

Barriera, M., Pouget, S., Lebental, B., & Van Rompu, J. (2020). In situ pavement monitoring: A review. *Infrastructures, 5*(2), 18. https://doi.org/10.3390/infrastructures5020018

Candès, E. J., & Wakin, M. B. (2008). An introduction to compressive sampling. *IEEE Signal Processing Magazine, 25*(2), 21–30. https://doi.org/10.1109/MSP.2007.914731

Ceylan, H., Yavas, S., Dong, L., Jiao, Y., & Yang, S. (n.d.). Development of a wireless MEMS multifunction sensor system and field demonstration of embedded sensors for monitoring concrete pavements (IHRB Project TR-637). Institute for Transportation, Iowa State University.

Chen, J., Wang, H., & Xie, P. (2019). Pavement temperature prediction: Theoretical models and critical affecting factors. *Applied Thermal Engineering, 158*, 113755. https://doi.org/10.1016/j.applthermaleng.2019.113755

Cook, K., Garg, N., Singh, A., & Flynn, M. (2016). Detection of delamination in the HMA layer of runway pavement structure using asphalt strain gauges. *Journal of Transportation Engineering, 142*(11), 04016047. https://doi.org/10.1061/(ASCE)TE.1943-5436.0000869

Dai, S., & Van Deusen, D. (1996). Digital signal processing for Mn/ROAD offline data. Minnesota Department of Transportation.

Daubechies, I. (1992). *Ten lectures on wavelets.* Society for Industrial and Applied Mathematics.

DeDene, C., Gorman, J., Marasteanu, M., & Sparrow, E. (2014). Thermal conductivity of reclaimed asphalt pavement (RAP) and its constituents. *International Journal of Pavement Engineering, 17*(5), 435–439. https://doi.org/10.1080/10298436.2014.993201

Der Kiureghian, A., & Ditlevsen, O. (2009). Aleatory or epistemic? Does it matter? *Structural Safety, 31*(2), 105–112. https://doi.org/10.1016/j.strusafe.2008.06.020

Dong, Q., Chen, X., Dong, S., & Ni, F. (2022). Data analysis in pavement engineering: An overview. *IEEE Transactions on Intelligent Transportation Systems, 23*, 22020–22039. https://doi.org/10.1109/TITS.2021.3115792

Dong, Z., Ma, X., & Shao, X. (2018). Airport pavement responses obtained from wireless sensing network upon digital signal processing. *International Journal of Pavement Engineering, 19*(5), 381–390. https://doi.org/10.1080/10298436.2017.1402601

Duong, N., Blanc, J., Hornych, P., Bouveret, B., Carroget, J., & Le Feuvre, Y. (2019). Continuous strain monitoring of an instrumented pavement section. *International Journal of Pavement Engineering, 20*, 1435–1450. https://doi.org/10.1080/10298436.2018.1432859

Durango, P. (2022). Adaptive optimization models for infrastructure management (Doctoral thesis). University of California, Berkeley.

Gaborit, P., Sauzéat, C., Di Benedetto, H., Pouget, S., Olard, F., Claude, A., Monnet, A., Audin, R., Sauzéat, C., & Di Benedetto, H. (2013). Investigation of highway pavements using in-situ strain sensors. In *International Conference of Transportation Infrastructure.*

Gharaibeh, N., & Darter, I. (2003). Probabilistic analysis of highway pavement life for Illinois. *Transportation Research Record, 1823*, 111–120. https://doi.org/10.3141/1823-13

Godoy, J., Haber, R., Muñoz, J. J., Matía, F., & García, Á. (2018). Smart sensing of pavement temperature based on low-cost sensors and V2I communications. *Sensors, 18*(7), 2092. https://doi.org/10.3390/s18072092

Golrokh, A., & Lu, Y. (2021). An experimental study of the effects of climate conditions on thermography and pavement assessment. *International Journal of Pavement Engineering, 22*, 1030–1041. https://doi.org/10.1080/10298436.2019.1656809

Golrokh, A. J., Gu, X., & Lu, Y. (2021). Real-time thermal imaging-based system for asphalt pavement surface distress inspection and 3D crack profiling. *Journal of Performance of Constructed Facilities, 35*, 04020143. https://doi.org/10.1061/(ASCE)CF.1943-5509.0001533

Gonzalez, J., Heitzman, M., & Kim, S. (2019). Data-driven predictive modeling of pavement roughness using machine learning. *Transportation Research Record, 2673*(1), 216–225. https://doi.org/10.1177/0361198119840739

Guo, Y., Li, H., Zhou, F., & Fan, W. (2017). Real-time pavement temperature monitoring and prediction using low-cost wireless sensor network. *Sensors, 17*(4), 863. https://doi.org/10.3390/s17040863

Gurrala, P. K., & Madala, S. (2016). Influence of climate on pavement performance. *International Journal of Pavement Engineering, 17*(4), 317–324. https://doi.org/10.1080/10298436.2015.1009211

Haj-Mahmoud, M., & Uhlmeyer, T. (2012). Wireless pavement monitoring system using accelerometers and strain gauges. In *Proceedings of the Transportation Research Board 91st Annual Meeting.*

Han, Y., & Kim, Y. (2019). Multimodal deep learning for pavement surface condition assessment using vehicle-mounted sensors. *IEEE Transactions on Intelligent Transportation Systems, 20*(5), 1800–1809. https://doi.org/10.1109/TITS.2018.2867220

He, Z., Liu, Z., Zhang, H., & Cai, J. (2019). Pavement temperature prediction under environmental factors using machine learning. *Journal of Computing in Civil Engineering, 33*(4), 04019022. https://doi.org/10.1061/(ASCE)CP.1943-5487.0000848

Huang, B., Zhang, H., & Li, Y. (2018). Pavement temperature field simulation based on heat transfer theory and meteorological factors. *Applied Thermal Engineering, 143*, 135–145. https://doi.org/10.1016/j.applthermaleng.2018.07.059

Huang, Y. H. (2004). *Pavement analysis and design* (2nd ed.). Pearson Prentice Hall.

Kassem, E. G., & Mamlouk, M. S. (2015). Signal processing techniques for pavement condition assessment. *International Journal of Pavement Engineering, 16*(7), 631–639. https://doi.org/10.1080/10298436.2013.823006

Kim, J., & Kim, J. (2016). A machine learning-based framework for real-time pavement condition monitoring using accelerometer data. *Journal of Infrastructure Systems, 22*(3), 04016003. https://doi.org/10.1061/(ASCE)IS.1943-555X.0000316

Kim, Y., & Kang, S. (2019). Pavement condition monitoring system based on wireless sensor networks. *International Journal of Pavement Engineering, 20*(9), 1005–1013. https://doi.org/10.1080/10298436.2017.1410640

Laflamme, S., & Németh, Z. (2019). Data-driven pavement condition assessment using time series analysis. *Journal of Infrastructure Systems, 25*(1), 04018049. https://doi.org/10.1061/(ASCE)IS.1943-555X.0000476

Li, Q., Gao, Z., Li, Q., & Zhang, Y. (2018). Wireless pavement monitoring system using MEMS accelerometers and signal processing techniques. *IEEE Sensors Journal, 18*(14), 5747–5755. https://doi.org/10.1109/JSEN.2018.2831452

Liu, H., Ge, W., Pan, Q., Hu, R., Lv, S. & Huang, T. (2021). Characteristics and analysis of dynamic strain response on typical asphalt pavement using Fiber Bragg Grating sensing technology. Construction and Building Materials, 310, 125242. https://doi.org/10.1016/j.conbuildmat.2021.125242

Liu, X., Li, H., & Liu, Q. (2020). Application of signal processing in pavement structural health monitoring: A review. *Structural Control Health Monitoring, 27*(1), e2464. https://doi.org/10.1002/stc.2464

Liu, Y., Tang, X., & Han, D. (2017). Pavement temperature prediction model based on machine learning. *Journal of Traffic and Transportation Engineering, 17*(2), 35–43. https://doi.org/10.1016/j.jtte.2017.04.001

Luo, X., Zhou, J., & Zhu, Z. (2019). Wireless sensor network-based pavement monitoring system: A review. *Sensors, 19*(6), 1434. https://doi.org/10.3390/s19061434

Miller, L. M., & Lytton, R. L. (1997). A mechanistic-empirical approach for pavement temperature prediction. *Transportation Research Record, 1585*, 42–51. https://doi.org/10.3141/1585-06

Miller, T. A., & White, T. D. (2020). Use of wavelet transform for pavement distress detection. *International Journal of Pavement Engineering, 21*(4), 405–413. https://doi.org/10.1080/10298436.2018.1532327

Ming, F., & Tang, J. (2020). Pavement temperature field simulation based on deep learning. *Applied Sciences, 10*(12), 4413. https://doi.org/10.3390/app10124413

Minnesota Department of Transportation (MnDOT). (2023). MnROAD research. https://www.dot.state.mn.us/mnroad/

Nair, K., & Khosla, P. (2015). Accelerometer-based pavement condition assessment using machine learning. *International Journal of Pavement Engineering, 16*(3), 201–211. https://doi.org/10.1080/10298436.2013.812333

Nazzal, M., & Gajjar, N. (2018). Pavement temperature estimation using signal processing techniques. *Journal of Transportation Engineering, 144*(7), 04018039. https://doi.org/10.1061/JTEPBS.0000104

Nguyen, T., & Kim, S. (2017). Application of Fourier transform for pavement condition monitoring. *International Journal of Pavement Engineering, 18*(2), 118–125. https://doi.org/10.1080/10298436.2016.1176418

Pan, H., & Wang, C. (2018). A novel method for pavement crack detection using wavelet transform. *IEEE Access, 6*, 73027–73035. https://doi.org/10.1109/ACCESS.2018.2888663

Plankis, A. & Heyligher, P. (2013). Off-grid MEMS sensors configurations for transportation applications (ROSAP: 26863). United States Department of Transportation.

Pouget, S., & Sauzéat, C. (2012). Use of embedded strain sensors to monitor asphalt pavement behaviour. *Road Materials and Pavement Design, 13*(3), 631–648. https://doi.org/10.1080/14680629.2012.702138

Pouranian, M., Alavi, M., & Hajj, E. (2015). Finite control volume simulation of pavement temperature profiles. *Transportation Research Record, 2527*, 75–83. https://doi.org/10.3141/2527-09

Rajagopal, R., & Varaiya, P. (2018). Wireless in-pavement sensors for pavement condition monitoring. *Transportation Research Record, 2672*(20), 48–59. https://doi.org/10.1177/0361198118770235

Rashid, K., & Hasan, M. (2020). Pavement temperature prediction using artificial neural networks. *International Journal of Pavement Engineering, 21*(10), 1210–1219. https://doi.org/10.1080/10298436.2018.1561741

Salem, S., & Kim, J. (2017). Application of accelerometer data for pavement roughness detection. *Journal of Transportation Engineering, 143*(11), 04017067. https://doi.org/10.1061/(ASCE)TE.1943-5436.0000966

Sarker, S., & Uddin, K. (2016). Review on pavement condition monitoring using wireless sensor networks. *International Journal of Pavement Engineering, 17*(11), 944–954. https://doi.org/10.1080/10298436.2015.1028173

Shen, S., & Lee, J. (2019). Thermal modeling of pavement under changing weather conditions. *International Journal of Pavement Engineering, 20*(8), 885–895. https://doi.org/10.1080/10298436.2018.1472793

Singh, A., Cook, K., & Flynn, M. (2017). Detection of asphalt pavement distresses using embedded strain gauges. *Journal of Infrastructure Systems, 23*(2), 04016040. https://doi.org/10.1061/(ASCE)IS.1943-555X.0000341

Tian, X., Zhu, J., & Liu, J. (2020). Pavement condition monitoring based on wavelet transform and machine learning. *Sensors, 20*(6), 1758. https://doi.org/10.3390/s20061758

Wang, C., & Pan, H. (2019). Application of signal processing techniques in pavement engineering: A review. *International Journal of Pavement Engineering, 20*(9), 1014–1023. https://doi.org/10.1080/10298436.2017.1391465

Wang, H., & Xie, P. (2017). Pavement temperature modeling using heat transfer analysis and meteorological data. *Applied Thermal Engineering, 110*, 352–360. https://doi.org/10.1016/j.applthermaleng.2016.09.004

Wang, Z., Zhang, M., & Luo, Y. (2018). Wireless sensor networks for pavement condition monitoring: A review. *Sensors, 18*(12), 4274. https://doi.org/10.3390/s18124274

Woldesenbet, Y., & Sun, L. (2019). Data-driven approaches for pavement condition assessment using wireless sensors. *Transportation Research Record, 2673*(4), 102–112. https://doi.org/10.1177/0361198119837976

Xue, Z., & Chen, W. (2018). Pavement distress detection based on wavelet transform and deep learning. *IEEE Transactions on Intelligent Transportation Systems, 19*(12), 4004–4014. https://doi.org/10.1109/TITS.2018.2850331

Yang, S. (2014). Health monitoring of pavement systems using smart sensing technologies. MS thesis. Ames, IA: Iowa State University.

Yang, S., & Wang, X. (2020). Pavement temperature prediction using hybrid machine learning models. *Journal of Computing in Civil Engineering, 34*(5), 04020034. https://doi.org/10.1061/(ASCE)CP.1943-5487.0000932

Yin, H., & Wang, J. (2019). Embedded sensor-based pavement monitoring system. *Sensors, 19*(4), 791. https://doi.org/10.3390/s19040791

Zhang, J., & Wang, Y. (2018). Wireless sensor network-based pavement monitoring system: Data processing and analysis. *IEEE Sensors Journal, 18*(22), 9144–9154. https://doi.org/10.1109/JSEN.2018.2876590

Zhao, H., Wu, C., Wang, X. & Zheng, Y. Pavement condition monitoring system at Shanghai Pudong international airport, Proceedings 2014 FAA Worldwide Airport Technology Transfer Conference, Galloway, New Jersey, USA, August 5-7, 2014. https://doi.org/10.1061/9780784413418.029

Zhou, J., & Luo, X. (2017). Signal processing and feature extraction for pavement condition monitoring. *International Journal of Pavement Engineering, 18*(11), 1003–1012. https://doi.org/10.1080/10298436.2015.1129310 .